



Kinetics of the tungsten hexafluoride-silane reaction for the chemical vapor deposition of tungsten
by Huseyin Gokce

A thesis submitted in partial fulfillment of the requirements for the degree of Doctor of Philosophy in
Chemical Engineering

Montana State University

© Copyright by Huseyin Gokce (1991)

Abstract:

Tungsten has been used for multilevel metallization in very large scale integration (VLSI) technology. Reduction by silane has been considered as a high-rate, low-temperature process alternative to hydrogen reduction of tungsten hexafluoride in the chemical vapor deposition of W. In the present study, the kinetics of the low pressure chemical vapor deposition (LPCVD) of tungsten by silane reduction of tungsten hexafluoride on Si(100) surfaces was studied.

A single-wafer, cold-wall reactor was used for the experiments. The SiH_4/WF_6 ratio was 1.0. The pressure and temperature range were 1-10 torr and 137-385°C, respectively. Kinetic data were obtained in the absence of mass transfer effects. The film thicknesses were measured by gravimetry. Scanning electron microscopy (SEM), Auger electron spectroscopy (AES), x-ray diffraction (XRD), and resistivity measurements were used to analyze the W films.

For the horizontal substrate position and 4-minute reaction times, the apparent activation energies were determined to be 0.35 eV/atom for 10 torr, 0.17 eV/atom for 3 torr, and 0.08 eV/atom for 1 torr. Lower temperatures and higher pressures produced porous films, while higher temperatures and lower pressures resulted in continuous films with smoother surfaces. At the Si-W interface, a W(110) preferential orientation was observed. As the W films grew thicker, W orientation switched from (110) to (100). Apparent activation energy seems to change with thickness.

Si and F contents of the films were within the noise level for Auger detection. Porosity was found to be influential in the film resistivity.

The higher activation energy observed at higher pressure was deduced to be a result of limitations in the rate of SiH_4 adsorption and subsequent adatom surface diffusion. The domination of W(100) orientation for thick films at high temperatures was attributed to a reconstruction of W(100) surfaces on which adatom surface diffusion is easier.

KINETICS OF THE TUNGSTEN HEXAFLUORIDE-SILANE REACTION
FOR THE CHEMICAL VAPOR DEPOSITION OF TUNGSTEN

by
Huseyin Gokce

A thesis submitted in partial fulfillment
of the requirements for the degree

of
Doctor of Philosophy
in
Chemical Engineering

MONTANA STATE UNIVERSITY
Bozeman, Montana

June 1991

D378
G5615

ii

APPROVAL

of a thesis submitted by

Huseyin Gokce

This thesis has been read by each member of the thesis committee and has been found to be satisfactory regarding content, English usage, format, citations, bibliographic style, and consistency, and is ready for submission to the College of Graduate Studies.

July 29, 1991
Date

John T. Sears
Chairperson, Graduate Committee

Approved for the Major Department

July 29, 1991
Date

John T. Sears
Head, Major Department


Approved for the College of Graduate Studies

August 6, 1991
Date

Henry L. Parsons
Graduate Dean

STATEMENT OF PERMISSION TO USE

In presenting this thesis in partial fulfillment of the requirements for a doctoral degree at Montana State University, I agree that the Library shall make it available to borrowers under rules of the Library. I further agree that copying of this thesis is allowable only for scholarly purposes, consistent with "fair use" as prescribed in the U.S. Copyright Law. Requests for extensive copying or reproduction of this thesis should be referred to University Microfilms International, 300 North Zeeb Road, Ann Arbor, Michigan 48106, to whom I have granted "the exclusive right to reproduce and distribute copies of the dissertation in and from microfilm and distribute by abstract in any format."

Signature 
Date July 29, 1991

Dedicated to my parents,
Habibe and Emin Gokce

ACKNOWLEDGEMENTS

I wish to express my deepest gratitude to Dr. John T. Sears for his guidance and encouragement throughout the course of this research. Likewise, I am indebted to Dr. Turgut Sahin for his continuous support and technical advice even after assuming a position in industry.

I wish to express my special thanks to Dr. Max C. Deibert and Dr. John F. Mandell of Chemical Engineering Department and Dr. Recep Avci of Physics Department at MSU for their helpful suggestions during this study.

My fellow graduate students and the staff of the Chemical Engineering Department have created a very pleasant working environment, I gratefully acknowledge their help and friendship. Lyman Fellows deserves special appreciation for his help in the maintenance of the equipment.

My thanks are due to Dr. William Inskeep of Plant and Soil Science at MSU for his help with the x-ray diffraction facility. This research would not have occurred without the silicon wafers supplied by Dr. Robert S. Blewer of Sandia National Laboratories, his help is gratefully acknowledged.

Financial support provided in part by Montana Science and Technology Alliance is acknowledged.

Last, but not the least, I would like to take this opportunity to thank my parents for their unending moral support, understanding and patience throughout this work.

TABLE OF CONTENTS

	Page
LIST OF TABLES.....	ix
LIST OF FIGURES.....	x
ABSTRACT.....	xiv
1. INTRODUCTION.....	1
Research Objective.....	3
2. LITERATURE SURVEY.....	5
Thin Films.....	5
Thin Film Formation.....	6
Condensation and Nucleation.....	7
Film Growth.....	13
The Island Stage.....	14
The Coalescence Stage.....	14
The Channel Stage.....	16
The Continuous Film.....	16
Growth Modes.....	17
Epitaxial Growth.....	19
Thin Film Analysis Techniques.....	20
X-ray Diffraction.....	20
Diffractometer Method.....	22
Sheet Resistance.....	23
Four-point Probe Method.....	23
Scanning Electron Microscopy.....	26
Auger Electron Spectroscopy.....	29
Film Thickness Measurement.....	34
Chemical Vapor Deposition.....	37
Basic Steps in CVD.....	38
Experimental Parameters in CVD.....	39
Deposition Temperature.....	39
Gas Flow Rate.....	44
Crystallographic Orientation.....	47
Substrate Position.....	48
Reactant Partial Pressure.....	49
Surface Area.....	49
Chemical Vapor Deposition Reactors.....	49
Hot-wall Reactors.....	50
Cold-wall Reactors.....	50
Atmospheric Pressure Reactors.....	50
Low-pressure CVD Reactors.....	52
Plasma-enhanced CVD Reactors.....	54
Photon-induced CVD Reactors.....	55
Chemical Vapor Deposition of Tungsten.....	56
Reactions for CVD of Tungsten.....	59
Si Reduction of WF_6	61

TABLE OF CONTENTS (Continued)

	Page
H ₂ Reduction of WF ₆	66
SiH ₄ Reduction of WF ₆	71
3. EXPERIMENTAL.....	85
Reaction System.....	84
Equipment.....	84
Gas Lines and Controllers.....	84
Reactor.....	86
Pressure Controller.....	89
Pumps.....	89
Effluent Gas Treatment.....	90
Oil Filtering System.....	91
Experimental Procedure.....	92
Sample Preparation.....	92
Deposition.....	92
Reactor Preparation.....	92
Reactor Operation.....	94
Data Analysis.....	94
Sheet Resistance Measurement.....	95
Film Thickness Measurement.....	95
SEM Analysis.....	96
AES Analysis.....	97
X-ray Diffraction Analysis.....	98
Scope of the Experiments.....	98
4. RESULTS.....	101
Preliminary Experiments.....	101
AES Analysis.....	104
Kinetics-Gravimetric.....	109
SEM Analysis.....	111
Time-dependent Experiments.....	111
Overgrown Films.....	119
4-Minute Experiments.....	121
X-ray Diffraction Analysis.....	128
Film Resistivity.....	133
5. DISCUSSION.....	138
Verification of Kinetic W Deposition.....	138
Impurity Content.....	138
Kinetic Region Gas Flow Rate.....	142
Effect of Substrate Position on Kinetics.....	145
Kinetics and Morphology.....	146
Morphology, Nucleation and Growth.....	146
Crystal Structure.....	151
Tungsten Growth on Si.....	152

TABLE OF CONTENTS (Continued)

	Page
Tungsten Growth on W.....	155
Crystallinity and Crystal Size.....	159
Proposed Kinetic Steps.....	163
Film Properties.....	173
Film Resistivity.....	173
Adhesion and Stress.....	175
6. SUMMARY AND CONCLUSIONS	178
7. RECOMMENDATIONS.....	182
REFERENCES CITED.....	186
APPENDICES.....	196
APPENDIX A-Potential Hazards of the Reaction Gases.....	197
Abbreviations.....	198
Hydrogen Fluoride (HF).....	198
Tungsten Hexafluoride (WF_6).....	199
Silicon Tetrafluoride (SiF_4).....	199
Hydrogen (H_2).....	199
Silane (SiH_4).....	199
Safety in the Reactor System.....	200
APPENDIX B-Calculation of Reactant Fractional Conversion.....	201
APPENDIX C-Prediction of Transport Properties for Reaction Gases.....	204
APPENDIX D-Reynolds Number Calculation.....	207
APPENDIX E-Sample Calculation for Mass Flux to the Substrate.....	212
APPENDIX F-X-ray Diffraction Line Data for Tungsten Phases.....	219
APPENDIX G-Tungsten Crystal Size Calculation.....	222
The Scherrer Formula.....	223
Sample Calculation for W Crystal Size.....	223
APPENDIX H-SEM Micrographs for Time-dependent Experiments.....	225

LIST OF TABLES

Table	Page
1. Free Energy Change at 600 K.....	60
2. Tungsten Phases and Their Properties.....	81
3. Specification of the Reaction Gases.....	86
4. AES Sensitivity Factors.....	97
5. Gas Flow Conditions.....	100
6. X-ray Diffraction Intensities of Tungsten Films.....	131
7. X-ray Diffraction Peak Widths of Tungsten Films.....	132
8. Lattice Mismatch, ϵ , Between Si and W Crystal Surfaces.....	153
9. Calculated Grain Sizes and Measured Aggregate Sizes for Tungsten Films.....	161
10. Tungsten Deposition Rates at 285°C, Experimental versus Theoretical at $X_{SiH_4} = 1.0$	167
11. Slopes for Sheet Resistance versus Inverse Deposition Time.....	175
12. Critical Properties for the Reactant Gases.....	205
13. Lennard Jones Parameters for the Reactant Gases.....	206
14. Transport Properties for the Reactant Gases at 285°C.....	206
15. Gas Phase Composition of the Reactant Gases.....	208
16. X-ray Diffraction Lines for α -W.....	220
17. X-ray Diffraction Lines for β -W.....	221
18. X-ray Diffraction Lines for W_3Si_5	221

LIST OF FIGURES

Figure	Page
1. Saturation density of nuclei vs. reciprocal temperature.....	12
2. (a) Schematic of the stages of film growth.....	15
(b) Schematic of the shape changes during coalescence.....	15
3. Various modes of growth of an overlayer on a substrate.....	18
4. Equivalence of a second order reflection.....	21
5. X-ray diffractometer configuration.....	21
6. Definition of sheet resistance.....	24
7. Schematic diagram for a four-point probe measuring setup.....	24
8. Positive and negative sources relative to point P.....	24
9. (a) Energy spectrum of electrons emitted from a surface bombarded by an electron beam. (b) The derivative of the number of emitted electrons with respect to the energy.....	27
10. Schematic drawing of a scanning electron microscope....	27
11. X-ray and Auger electron emission during de-excitation of atom after initial ionization.....	30
12. Auger spectrum of W film surface on Si.....	33
13. Temperature dependence of growth rate for CVD films....	42
14. Reaction rate as a function of reciprocal temperature for zero and negative heat of reaction.....	43
15. Reaction rate as a function of reciprocal temperature for positive heat of reaction.....	45
16. Idealized growth-rate versus fluid flow-rate plot showing the different growth regimes.....	46
17. Schematic diagrams of CVD reactors.....	51
18. Address access time as a function of gate length.....	57

LIST OF FIGURES (Continued)

Figure	Page
19. Future applications of refractory metals and/or metal silicides.....	59
20. Schematic illustration of several problems associated with selective W deposition by LPCVD.....	62
21. Arrhenius plot of deposition rate of CVD tungsten by H_2 reduction of WF_6	68
22. Normalized x-ray texture as a function of film thickness.....	72
23. Arrhenius plot for SiH_4 - WF_6 reaction system [7].....	74
24. Arrhenius plot of H_2 and SiH_{2n+2} ($n = 1-3$) reduction of WF_6 [8].....	74
25. Arrhenius plot for $SiH_4/WF_6 < 0.9$ [9].....	76
26. Arrhenius plot of blanket W deposition [10].....	76
27. Schematic diagram of the LPCVD reaction system.....	85
28. Cross-sectional view of the LPCVD reactor.....	88
29. Preliminary experiments to assure differential reactor.....	103
30. Auger depth profile for W film deposited at 10 torr and $137^\circ C$	105
31. Auger depth profile for W film deposited at 1 torr and $137^\circ C$	106
32. Auger depth profile for W film deposited at 3 torr and $385^\circ C$	107
33. Arrhenius plot for WF_6 - SiH_4 system. Substrate horizontal.....	110
34. Arrhenius plot for WF_6 - SiH_4 system. Substrate vertical.....	112
35. SEM micrographs of W surfaces at different reaction times.....	114

LIST OF FIGURES (Continued)

Figure	Page
36. SEM micrographs of W surfaces, t = 1.5 min, P = 10 torr.....	115
37. SEM micrographs of W surfaces, t = 1.5 min, P = 1 torr.....	116
38. Aggregate growth rate, parallel to surface, P = 10 torr.....	117
39. Aggregate growth rate, parallel to surface, P = 1 torr.....	118
40. Arrhenius plot for W aggregate growth.....	120
41. SEM micrographs of tungsten surfaces, t = 12 min.....	122
42. SEM micrographs of tungsten surfaces, t = 10 min.....	123
43. SEM cross-sectional view of tungsten film, t = 12 min.....	124
44. SEM cross-sectional views of tungsten films, t = 10 min.....	125
45. SEM surface micrographs of W deposited at 385°C.....	126
46. SEM surface micrographs of W deposited at 137°C.....	127
47. X-ray diffraction patterns of W films deposited at T = 285°C and P = 1 torr.....	130
48. Resistivity versus W film thickness.....	134
49. Sheet resistance versus inverse deposition time for P = 10 torr.....	136
50. Sheet resistance versus inverse deposition time for P = 1 torr.....	137
51. Schematic diagrams of W(100) surfaces.....	158
52. The mosaic structure of a real crystal.....	162
53. Arrhenius plots for adsorption of silane on Si(111)-(7x7).....	169
54. SEM micrographs of W surfaces deposited at different reaction times, P = 10 torr, T = 285°C.....	226

LIST OF FIGURES (Continued)

Figure	Page
55. SEM micrographs of W surfaces deposited at different reaction times, P = 10 torr, T = 330°C.....	227
56. SEM micrographs of W surfaces deposited at different reaction times, P = 10 torr, T = 385°C.....	228
57. SEM micrographs of W surfaces deposited at different reaction times, P = 1 torr, T = 285°C.....	229
58. SEM micrographs of W surfaces deposited at different reaction times, P = 1 torr, T = 330°C.....	230
59. SEM micrographs of W surfaces deposited at different reaction times, P = 1 torr, T = 385°C.....	231

ABSTRACT

Tungsten has been used for multilevel metallization in very large scale integration (VLSI) technology. Reduction by silane has been considered as a high-rate, low-temperature process alternative to hydrogen reduction of tungsten hexafluoride in the chemical vapor deposition of W. In the present study, the kinetics of the low pressure chemical vapor deposition (LPCVD) of tungsten by silane reduction of tungsten hexafluoride on Si(100) surfaces was studied.

A single-wafer, cold-wall reactor was used for the experiments. The SiH_4/WF_6 ratio was 1.0. The pressure and temperature range were 1-10 torr and 137-385°C, respectively. Kinetic data were obtained in the absence of mass transfer effects. The film thicknesses were measured by gravimetry. Scanning electron microscopy (SEM), Auger electron spectroscopy (AES), x-ray diffraction (XRD), and resistivity measurements were used to analyze the W films.

For the horizontal substrate position and 4-minute reaction times, the apparent activation energies were determined to be 0.35 eV/atom for 10 torr, 0.17 eV/atom for 3 torr, and 0.08 eV/atom for 1 torr. Lower temperatures and higher pressures produced porous films, while higher temperatures and lower pressures resulted in continuous films with smoother surfaces. At the Si-W interface, a W(110) preferential orientation was observed. As the W films grew thicker, W orientation switched from (110) to (100). Apparent activation energy seems to change with thickness.

Si and F contents of the films were within the noise level for Auger detection. Porosity was found to be influential in the film resistivity.

The higher activation energy observed at higher pressure was deduced to be a result of limitations in the rate of SiH_4 adsorption and subsequent adatom surface diffusion. The domination of W(100) orientation for thick films at high temperatures was attributed to a reconstruction of W(100) surfaces on which adatom surface diffusion is easier.

CHAPTER 1

INTRODUCTION

In the mid 1970's, very large scale integration (VLSI) technology started with 64Kbit dynamic random access memory for dynamic memory devices and specific integrated circuits. The technology has recently improved to provide 16Mbit capacities. It is predicted that at the end of the 20th century, dynamic memory chips will reach 1 gigabit capacity [1]. This much memory is only one-tenth of the number of neurons in a human brain. Thus, one memory board would be equivalent to a human brain in terms of data storage.

The developments in the VLSI technology have been making ultra-large scale integration (ULSI) technology a coming reality, as submicron dimensions can be utilized. Such a transmutation in the technology has certain requirements. Some of them include high aspect via-contacts, complicated geometry in multi-level interconnections, high current density, and shallow junctions at source/drain regions. These requirements have directed the researchers to look for new materials which can provide low contact resistance, smooth interconnections to prevent electromigration, and low temperature processibility.

It has been shown that selectively deposited tungsten (1,000 - 1,500 Å) on monosilicon or polysilicon surfaces in metal-oxide silicon (MOS) device structures can serve as an

interconnect shunt and contact diffusion barrier [2]. The term "selective deposition" is used when tungsten (W) is deposited only onto silicon (Si) and surrounding silicon dioxide (SiO_2) is free of deposition.

Tungsten hexafluoride, a commonly used source gas for tungsten deposition, can be reduced by either silane, hydrogen or silicon substrate itself. The kinetics for tungsten deposition by Si and H_2 reduction of WF_6 has been studied extensively and the parameters have been well established [3-6]. The Si reduction reaction causes the consumption of the silicon substrate and produces very rough W-Si interfaces. The deposition reaction stops after a limiting W film thickness is reached ($\sim 300 - 400 \text{ \AA}$). H_2 reduction reaction does not show a self-limiting behavior but has some drawbacks, such as silicon consumption of the substrate which appears in the form of tunnels and required high deposition temperatures for practical deposition rates.

Chemical vapor deposition (CVD) of tungsten by hydrogen (H_2) reduction of tungsten hexafluoride (WF_6) is considered to be a potential technique for integrated-circuit applications. Low pressure chemical vapor deposition (LPCVD) has some proven advantages over atmospheric pressure CVD. These advantages are increased control over the deposition ambient, greater throughput, lower reactant gas flows, high purity deposits, and excellent deposit uniformities and conformities.

Silane (SiH_4) reduction of WF_6 was shown to suppress silicon consumption and tunneling [7,8]. Therefore, the leakage current and contact resistance is low, which are the desired electrical properties. Kinetic studies on the LPCVD of tungsten using SiH_4 - WF_6 reaction system have been very limited since most studies aimed at developing a better tungsten film quality rather than establishing the kinetic parameters [7-10]. All the researchers have observed a complicated behavior in the temperature dependence of the kinetics of the SiH_4 - WF_6 reaction, and thus, no Arrhenius activation energies have been reported.

Research Objective

An efficient design for a commercial production system requires knowledge of reaction kinetic parameters. The lack of kinetic parameters for the SiH_4 - WF_6 system is the motivation for this study. The research objectives are:

- (1) To measure and evaluate kinetic data for the chemical vapor deposition of tungsten by SiH_4 reduction of WF_6 . The substrate surface is to be Si(100) and the kinetic data will be acquired under differential reactor conditions. The deposition rates will be determined by a gravimetric method.
- (2) To examine the quality of the tungsten films deposited by the WF_6 - SiH_4 reaction. Thin W films will be analyzed with

scanning electron microscopy (SEM), x-ray diffraction (XRD), Auger electron spectroscopy (AES), and resistivity measurements.

- (3) To interpret the kinetic data in the context of the morphology and crystal structure studies. Parameters are the reaction temperature and pressure, the gas flow rate, the film morphology, and the crystal orientation.

CHAPTER 2

LITERATURE SURVEY

Thin Films

VLSI devices use a variety of thin films as metals, semiconductors, and insulators. A better understanding of chemical and physical properties of thin films is essential to improve the device performance. There are specific methods developed to form thin films for different applications [11]. Regardless of the method of formation, VLSI fabrication requires that the process be economical and the resultant film have the following properties [12]:

- Good thickness uniformity.
- High purity and high density to provide good insulation (or conduction) and integrity.
- Controlled composition and stoichiometries.
- High degree of structural perfection to ensure film continuity over the lifetime of the device.
- Good electrical properties.
- Excellent adhesion and low stress values to eschew film discontinuity due to deformation, cracking, undercutting, and lifting effects.
- Good step coverage.

It is known that the properties of a thin film may be quite different from those of the bulk material. These differences are more pronounced as the film thickness gets extremely small, namely at the micron level. For one thing, thin films have a higher surface-to-volume ratio than a bulk material which makes the surface properties more influential on the film properties. For another, the peculiar structure of the thin film is an important factor in determining the film properties, and this structure is dictated by the nature of the processes which occur during film formation.

Thin Film Formation

Thin films can be formed by a large variety of techniques [13]. In VLSI fabrication, the formation of thin films can be categorized into two major procedures:

- (1) Film growth by interaction of a vapor-deposited species with the substrate.
- (2) Film formation without causing changes to the substrate.

The first category includes thermal oxidation and nitridation of single crystal silicon and polysilicon substrates, and the formation of silicides by direct reaction of a predeposited metal and the substrate.

The second category includes three forms of deposition on the substrate:

i) Chemical vapor deposition (CVD), where solid films are deposited on a substrate by reacting vapor phase chemicals on the substrate surface. Amorphous, polycrystalline and single-crystalline films can be formed by CVD. The process is called epitaxy when CVD is used to form single-crystal thin films.

ii) Physical vapor deposition (PVD), where the atoms of the material to be deposited are physically dislodged from a source material into vacuum, then the condensation occurs on the substrate to form the thin film. PVD processes include evaporation, sputtering and molecular beam epitaxy.

iii) The deposition of a liquid on a substrate which is then dried to form the solid thin film. Spin-coating is the most commonly used technique.

Thin film deposition by most common processes, such as PVD and CVD, involves a condensation transformation from the vapor to the solid phase. The formation of a thin film can be best understood by the thermodynamic and kinetic analysis of the condensation phenomena [14,15].

Condensation and Nucleation

The initial step of thin film nucleation in CVD and PVD is the impingement of vapor molecules onto the substrate. After impingement, the vapor molecules can either adsorb and stick permanently to the substrate, or they adsorb momentarily and re-evaporate, or they ricochet back to the vapor phase.

The initial attraction of the impinging atom (or molecule) requires that instantaneous dipole or quadrupole moments of the surface atoms exist. The excess energy of the attracted atom is transferred to the substrate in the form of lattice oscillations. The attracted atom then becomes attached to the surface after losing its velocity component normal to the surface. The attachment of impinging vapor atoms on the surface is known as "adsorption" and the adsorbed atom is called "adatom".

Two types of adsorption phenomena have been recognized in principle:

i) Physisorption caused by secondary (van der Waals) attractive forces.

ii) Chemisorption caused by chemical bonding involving transfer of electrons between adsorbent and adsorbate.

Because of the nature of the bonding involved, physisorption is associated with much smaller binding energies (~ 0.25 eV) than is chemisorption (8-10 eV).

Adsorbent surfaces may be pictured as an array of adsorption sites where each adsorbed molecule occupies a minimum potential energy site [16]. An adsorbed atom may retain its initial lateral momentum or may be activated thermally from the surface so that it will jump over the energy barriers into the next available adsorption site. It is also possible that some of the adatoms re-evaporate from the surface into the vapor phase. The factors that affect the

rates of adsorption and desorption (re-evaporation) are given by the functions below, in which the variables are assumed separable. Then rate of adsorption, μ_a , is [17]

$$\mu_a = \frac{P}{\sqrt{2\pi mkT}} \sum_{i=1}^m n_i \sigma_i f(\theta_i) e^{-E_i/RT} \quad (1)$$

and rate of desorption, μ_d , is

$$\mu_d = \sum_{i=1}^m n_i K_i f'(\theta_i) e^{-E'_i/RT} \quad (2)$$

where,

m : number of types of sites.

n_i : number of sites of type (i).

θ : surface coverage.

$f(\theta)$, $f'(\theta)$: function for the surface coverage dependence of adsorption and desorption, respectively.

R : gas constant.

E , E' : activation energy of adsorption and desorption, respectively.

σ , K : condensation and evaporation probability, respectively.

$P/(2\pi mkT)^{0.5}$: number of collisions with a surface

(m : mass of atom, k : Boltzmann constant).

Equations 1 and 2 indicate that adsorption rate is a function of both pressure, P , and temperature, T , while desorption rate is not influenced by pressure, but by temperature.

As the adatoms migrate along the surface, they collide with other atoms and form clusters of adsorbed atoms. The

small clusters consist of only a few atoms and have very high surface-to-volume ratios. This results in high surface energy values and energetically unstable clusters which have a high tendency to re-evaporate. For this reason, most theories on condensation and nucleation define a critical radius for clusters above which the total free energy of the system decreases with increasing radius. Hence, clusters larger than this critical size are stable and favor a continued growth. The stable clusters are called "nuclei" and the mechanism of their formation is termed "nucleation".

There are two basic models to explain the nucleation phenomena: the capillarity model which employs simple idealized geometrical shapes for the cluster [18,19], and the atomistic (or statistical) model [20] which uses only discrete arrangements of atoms. Furthermore, the capillarity model predicts a continuous variation of crystal size and nucleation rate with the degree of supersaturation, whereas the atomistic model predicts discontinuous changes which are more pronounced for smaller critical cluster sizes. In the limit of large critical nuclei, the two models become identical.

In the initial stages of condensation, clusters of various sizes are in metastable equilibrium with free adatoms. As the clusters grow to supercritical dimensions, they deplete the adatoms within their surrounding regions in which any further cluster formation (or nucleation) is not possible. These regions are called "capture zones".

It is observed that the film mass deposited depends on the total impingement time, the substrate temperature, the diffusion coefficient of adatoms on the surface, the mean residence time of adatoms, and the impingement rate [21]. The "onset" of condensation is defined by the initial formation of nuclei and is marked experimentally by the appearance of some observable mass of condensate on the substrate. The corresponding substrate temperature is called the "critical" condensation temperature. The critical temperature, T_c , however, depends on the observation time. If the adatoms have long enough mean free residence times of adherence on the surface at temperature T_c , all impinged atoms will be captured by stable nuclei so that the sticking coefficient will be unity even initially. For temperatures greater than T_c , the adatoms have less residence time on the surface due to increased desorption from the surface, therefore longer times are required for the onset of condensation.

Lewis and Campbell [22] have analyzed the nucleation process near T_0 for the case of the smallest possible critical nucleus. Figure 1 shows how the saturation density of nuclei changes with temperature and identifies incomplete and complete condensation temperature regions. At low temperatures or high impingement rates (complete condensation), the

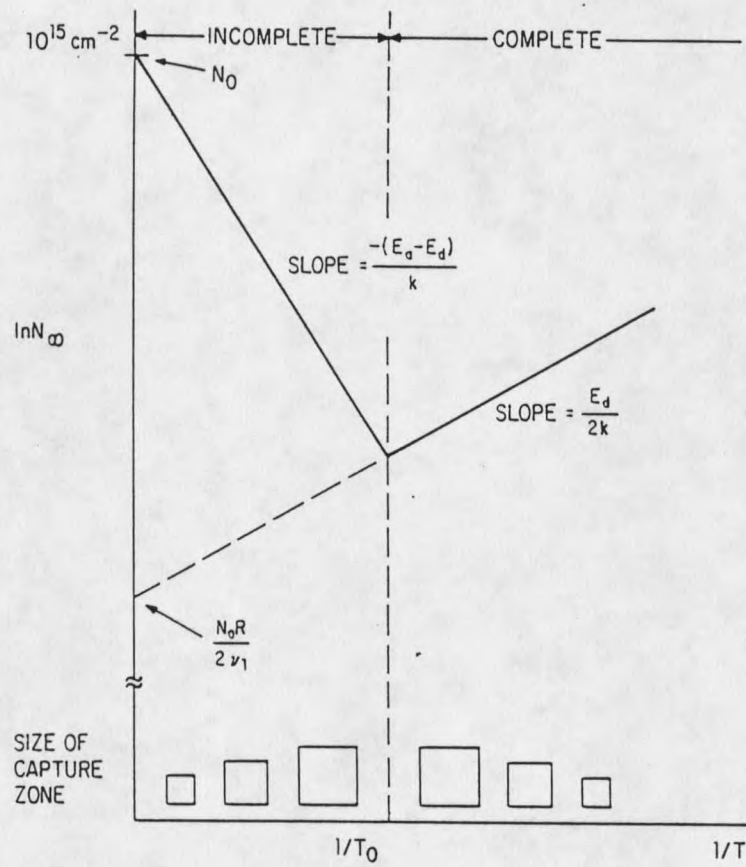


Figure 1. Saturation density of nuclei vs. reciprocal temperature, illustrating the boundary between initially complete and incomplete condensation [22].

impinged atoms immediately form stable pairs of density N_0 without the possibility of re-evaporation. In this region, the slope of the $\ln N_0$ vs. $1/T$ plot is positive since the diffusion coefficient increases with increasing temperature, hence increasing the size of the capture zone where further nucleation is not possible. At high temperatures (incomplete condensation), the slope is negative because increased temperatures lead to re-evaporation of adatoms which means smaller mean residence times. The result is decreased size of the capture zone around each nucleus, yielding more nuclei on the substrate.

Zinsmeister [23] has claimed that the desorption and evaporation of clusters, as well as adatoms, are not negligible in spite of the much greater activation energy involved. He indicated that at the beginning of the condensation, adatoms and very small clusters predominate, but later most of the condensate is tied up in larger clusters. He also showed that the sticking coefficient is low at the beginning of the condensation.

Film Growth

Electron-microscopic studies have revealed the different stages of film growth. Pashley, et al. [24] have identified the four basic stages of the growth process, namely, nucleation and island structure, coalescence of islands,

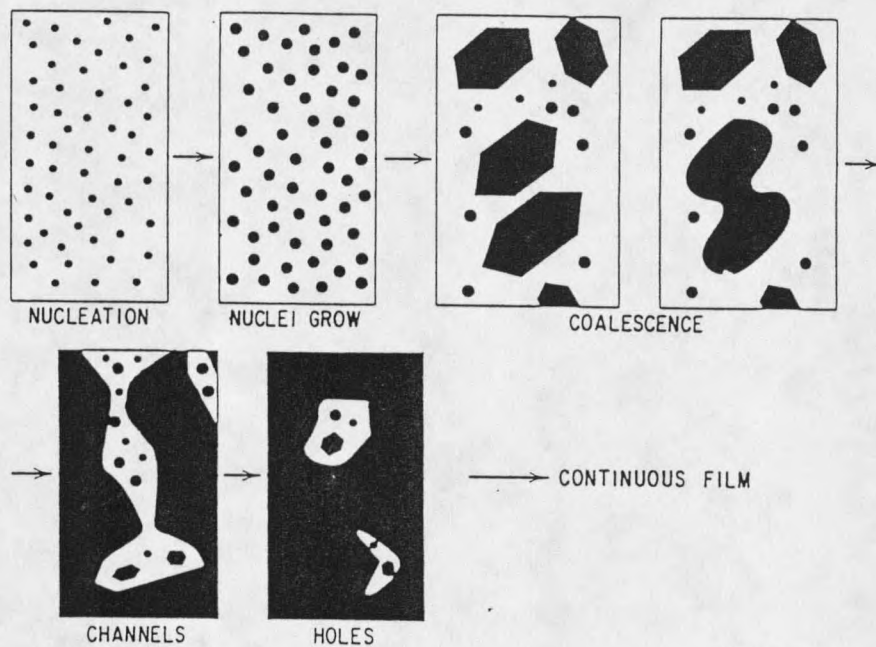
channel formation, and the formation of the continuous film. These stages are shown in Figure 2a and 2b and explained in the following sections [14].

(1) The Island Stage: Upon the onset of condensation, the initial nuclei are fairly uniform in size. Although the growth is three-dimensional in nature, the growth parallel to the substrate is greater than that normal to it. This implies growth as a result of surface diffusion of adatoms rather than growth by direct impingement.

(2) The Coalescence Stage: As two neighbor nuclei grow, at some point they touch each other and a liquid-like coalescence occurs as shown in Figure 2b. The driving force for coalescence is the reduction of surface energy by the formation of a new composite island which has a smaller surface-to-volume ratio.

A triangular, straight edged shape of the crystallites is characteristic of the late nucleation stage (Figure 2a). During coalescence, these well-defined crystallographic shapes become rounded. Mass transfer may occur by both volume and surface diffusion, but surface diffusion is shown to be the predominant mode. Curvature differences on the surface of the coalescing islands create surface tension forces, which drive atoms on the surface from convex-shaped regions to concave-shaped regions. These forces

(a)



(b)

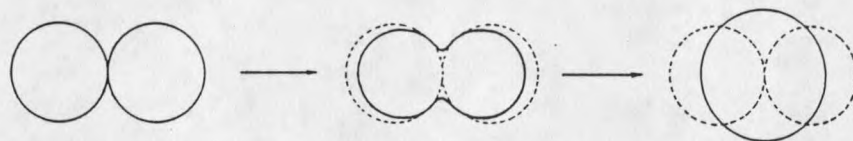


Figure 2. (a) Schematic of the stages of film growth.
 (b) Schematic of the shape changes during coalescence [24].

are minimized at the end by the formation of a rounded island. As a result, a reduction in area and an increase in height occur which, in turn, reduce the total substrate area covered by the islands.

In addition to surface area reduction, the surface energy is also reduced by rearranging the crystal orientation. After coalescence, preferred boundary planes are observed and the composite island assumes a hexagonal shape.

(3) The Channel Stage: During each coalescence, the smaller nuclei are pulled into more massive regions of the film leaving fresh substrate area for further secondary nucleation. As the islands grow and coalescence takes place continually, the islands become elongated and form larger islands separated by long channels or holes. The channels contain many secondary nuclei, which coalesce with each other and with the main film, thus increasing the main film mass and leaving fresh substrate areas behind for further secondary nucleation. Each repetition of this process makes the channel smaller and the cycle continues until the channel is filled in.

(4) The Continuous Film: Pashley et al. [24] observed that during film growth, especially in the coalescence stage, island orientation changes by recrystallization. A considerable degree of recrystallization occurs even at room

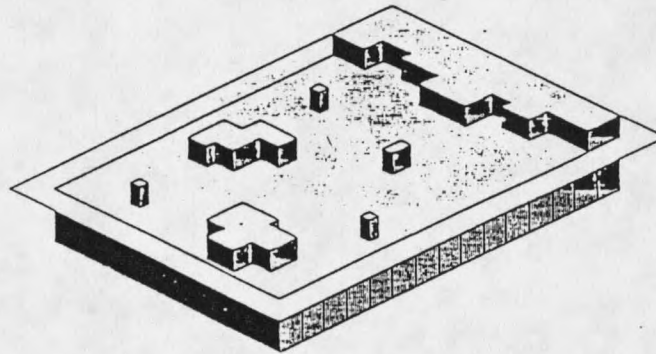
temperature. Each grain in a polycrystalline film incorporates a very large number of initial nuclei. Thus, the resulting number of crystals in a continuous film is significantly less than the initial number of nuclei.

Growth Modes

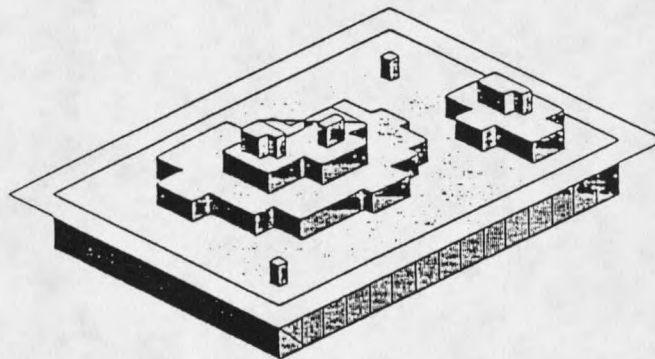
Three basic growth modes are recognized and named after the authors who established them: the Frank-van der Merwe (FM), the Stranski-Krastanov (SK), and Volmer-Weber (VW) modes [25]. These modes are illustrated in Figure 3. Bauer [26,27] has demonstrated that relative surface energies dictate the growth mode. Neglecting edge energies and the shape and size dependence of the surface energies, the equation governing the growth mode is

$$\Delta = \sigma_f + \sigma_i - \sigma_s \quad (3)$$

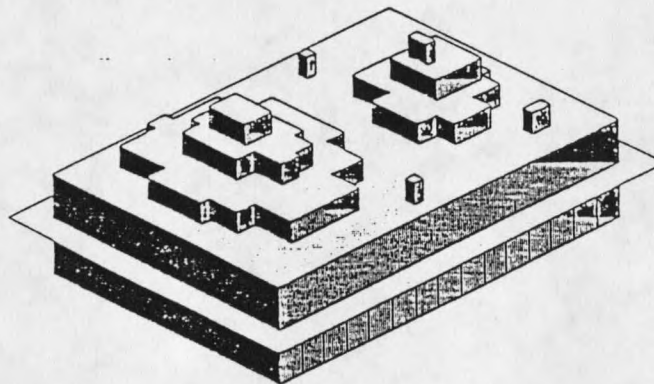
where, σ_f and σ_s are the specific free surface energies of film and substrate, respectively, and σ_i is the specific free interfacial energy. If the deposited material has a higher surface energy than the substrate ($\Delta > 0$), the film will tend to form a three-dimensional structure (VW mode), otherwise a layer by layer growth (FM mode) is favored ($\Delta \leq 0$). When σ_i changes with the size and shape of the island as the layers grow, transitions between the two modes occur and 3-D crystals grow on top of one or a few monolayers (SK mode).



(a)



(b)



(c)

Figure 3. Various modes of growth of an overlayer on a substrate: (a) Frank-van der Merwe, (b) Volmer-Weber, and (c) Stranski-Krastanov growth. The horizontal plane indicates where the substrate ends [25].

Epitaxial Growth

Epitaxy: from the Greek, $\epsilon\pi\iota$ (epi: placed or resting upon) + $\tau\alpha\chi\iota\zeta$ (taxis: arrangement). Epitaxy = "the growth of crystals on a crystalline substrate that determines their orientation" [25].

Frankemheim [28] pioneered the science of epitaxy by demonstrating that sodium nitrate can be grown from a solution onto a calcite crystal with a unique orientation relationship. Royer [29] used x-ray diffraction (XRD) to show that such oriented growth requires that lattice planes in both materials have similar structure and orientation to the substrate material; he concluded that epitaxial growth requires a lattice misfit of not more than about 15%. Lattice misfit, ϵ , is defined by

$$\epsilon = \frac{b - a}{a} \quad (4)$$

where, a and b are the in-plane lattice constants of substrate and overgrowth, respectively. Thus the occurrence of epitaxial growth is probable whenever the substrate and overgrowth have coincident lattices and low interfacial energy. Lattice mismatch causes a strain at the substrate-overgrowth interface. This strain is relieved by creating misfit dislocations in the overgrowth at the interface. Studies have been carried out to identify and characterize misfit dislocations at epitaxial interfaces [27,30].

Thin Film Analysis Techniques

X-ray Diffraction

As a crystallographic analysis method, x-ray diffraction is used for determining substrate orientation, for characterizing crystalline phases and preferred orientations in crystalline layers, and for identifying amorphous regions [31].

X-ray diffraction utilizes the following geometrical arrangements as illustrated in Figure 4:

- (1) The incident beam, the normal to the reflecting plane, and the diffracted beam are always on the same plane.
- (2) The angle between the diffracted beam and the transmitted beam is 2θ .

Diffraction occurs when the wavelength of the incident beam matches with the repeat distance between scattering centers to form a constructive interference. The criterion to be met for the Bragg law is

$$n\lambda = 2d\sin\theta \quad (5)$$

where, λ is the x-ray wavelength, d is the interplanar spacing, θ is the Bragg diffraction angle, and n is an integer giving the order of the diffraction. This geometry is illustrated in Figure 4. The experimentally measured angle is usually the diffraction angle, 2θ , rather than θ .

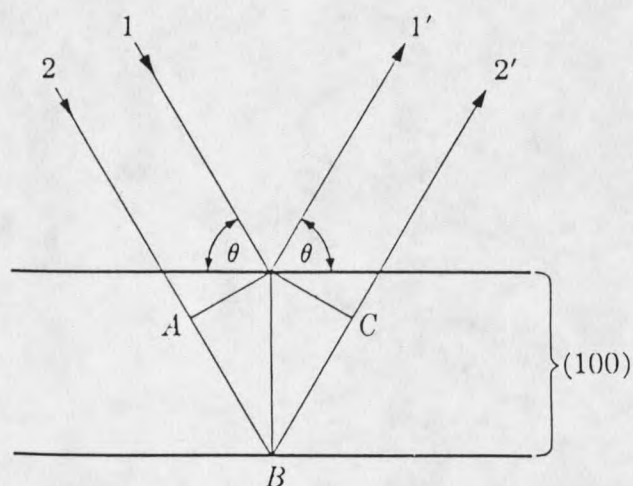


Figure 4. Equivalence of a second order reflection [31].

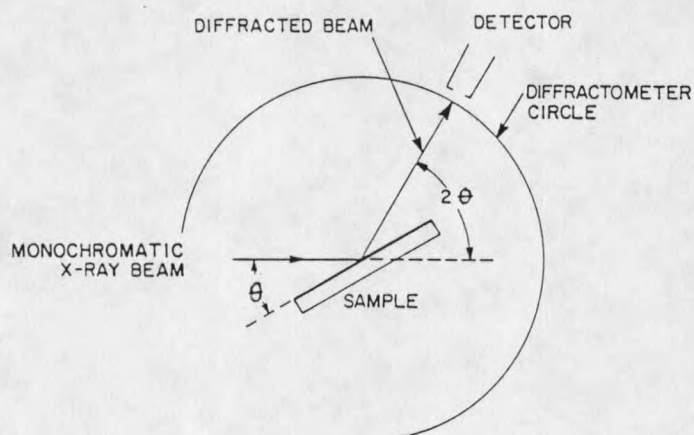


Figure 5. X-ray diffractometer configuration. As the sample rotates over an angle θ the detector moves along a circumference an angular distance 2θ ; a diffraction maximum occurs when θ is equivalent to a Bragg angle [32].

Four types of x-ray diffraction are commonly employed in VLSI fabrication processes; the Laue technique, the Read camera technique, the Huber-Seemann-Bohlin, and diffractometer methods. All these methods are based on establishing conditions that satisfy the Bragg requirement. More precise measurements of lattice parameters are obtained using a diffractometer geometry [32].

Diffractometer Method: The x-ray spectrometer is called a diffractometer when it is used with x-rays of known wavelength to determine the unknown spacing of crystal planes [31]. As a spectrometer, it is used to determine unknown wavelengths from crystal planes of known spacing. A diffractometer is shown in Figure 5 [32]. A monochromatic x-ray beam strikes the film surface at an angle θ . As the sample is slowly rotated, the detector is also rotated along the circumference of a circle with the same center as the sample. The detector moves in concert with the sample to maintain the diffraction angle, 2θ , at all times. Diffraction peaks appear wherever θ coincides with a Bragg angle. Data are usually recorded on a strip chart recorder as diffraction intensity, I , versus diffraction angle, 2θ . Then, the obtained diffraction pattern is matched with the patterns recorded in the ASTM Powder Diffraction Data File [33] for identification of the crystal structure.

Sheet Resistance

Sheet resistance values are used to electrically characterize the thin films in silicon microcircuits [34]. Consider a rectangle of a layer of length ℓ , width b , and thickness t as shown in Figure 6 [35]. The resistance measured in the direction parallel to the film is

$$R_s = \rho \frac{\ell}{bt} \quad (6)$$

where, ρ the resistivity of the film. If ℓ and b are sufficiently large or equal to each other, Equation (6) becomes

$$R_s = \frac{\rho}{t} \quad (7)$$

and is defined as sheet resistance of the film in ohm/square (Ω/\square). R_s is then independent of the size of the square but dependent on the film resistivity and film thickness. When the thickness and sheet resistance are measured, the film resistivity can be calculated by

$$\rho = R_s t. \quad (8)$$

Four-point Probe Method: Among the several techniques for measuring sheet resistance, the four-point probe method is widely used [36]. Figure 7 schematically shows a four-point probe measuring set-up. The probes are placed colinearly, with an equal spacing of a . A reference current I is forced between the outer two probes and the resulting voltage drop V is

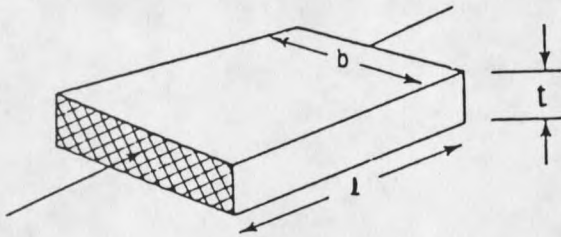


Figure 6. Definition of sheet resistance [35].

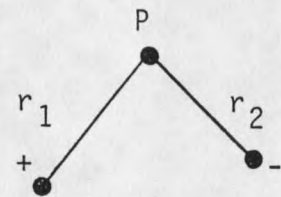


Figure 8. Positive and negative sources relative to point P.

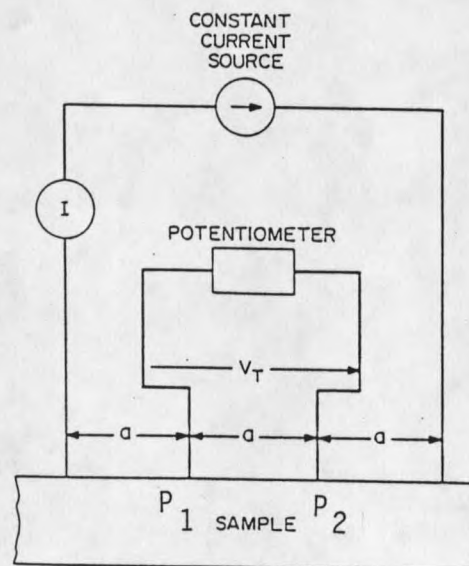


Figure 7. Schematic diagram for a four-point probe measuring setup.

measured between the inner probes. Consider a configuration in Figure 8. Point P is located at a distance r_1 to positive the source of current. If the layer has infinite dimensions, the potential, ψ , at point P is given by

$$\psi = \frac{IR_s}{2\pi} \ln \frac{r_2}{r_1} + A \quad (9)$$

where A is a constant of integration and I is the current. In the case of a four-point probe configuration (Figure 7) the potentials, ψ_1 and ψ_2 at points P_1 and P_2 can be expressed as

$$\psi_1 = \frac{IR_s}{2\pi} \ln 2 + A \quad (10)$$

and

$$\psi_2 = \frac{-IR_s}{2\pi} \ln 2 + A \quad (11)$$

Then, the resulting potential difference between P_1 and P_2 can be calculated by

$$\psi_1 - \psi_2 = V = \frac{IR_s}{\pi} \ln 2 \quad (12)$$

Thus, the sheet resistance is

$$R_s = \left(\frac{\pi}{\ln 2} \right) \frac{V}{I} \quad (13)$$

and

$$R_s = 4.5324 \frac{V}{I} \quad (14)$$

Hence, for an infinite sheet, the sheet resistance can be directly calculated from the V/I ratio. For the samples with finite dimensions Equation 14 can be generalized as

$$R_s = C \frac{V}{I} \quad (15)$$

where C is a correction factor and is a function of the probe spacing and sheet dimensions [37].

Scanning Electron Microscopy

Scanning electron microscopy (SEM) is a standard analysis tool in VLSI laboratories because of its superiority over optical microscopy [38,39]. A magnification of 100,000X with a spatial resolution better than 100 Å can be obtained with SEM, whereas for optical microscopes, these figures are 1,000X and 10,000 Å, respectively. SEM can give a depth of field of 2-4 μm at 10,000X magnification and 0.2-0.4 mm at 100X magnification which are much deeper than those of optical microscopes. Thus, SEM provides information on line width, film thickness, step coverage, edge profiles after etch, and other morphology data for VLSI device surfaces.

In an analogous manner to light, when an electron interacts with a specimen, the electron can be partially or completely transmitted, partially or completely absorbed, or scattered by reflection and refraction. Absorption may result in fluorescence, phosphorescence, heating of the specimen, the ejection of photoelectrons, or a combination of these. Figure 9 shows the energy distribution of electrons emitted from a surface bombarded by an electron beam of energy E_0 .

Three predominant electron emissions are observed.

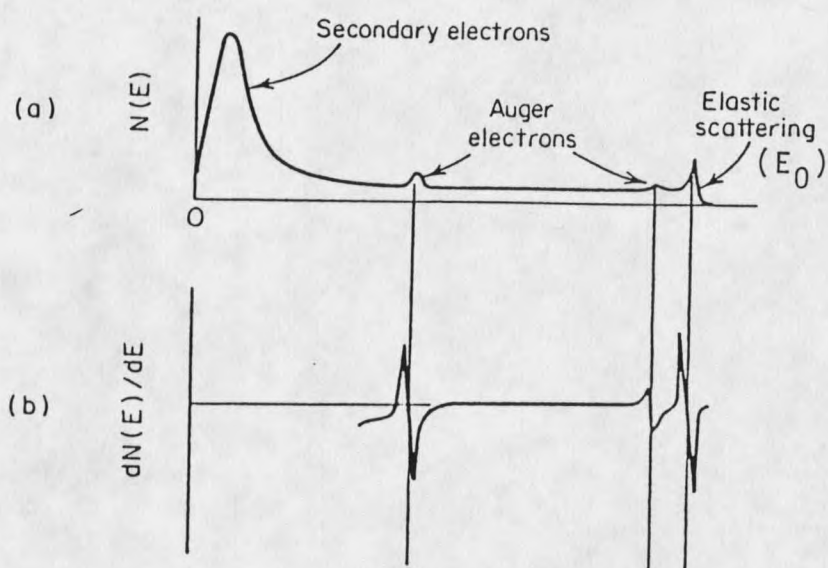


Figure 9. (a) Energy spectrum of electrons emitted from a surface bombarded by an electron beam. (b) The derivative of the number of emitted electrons with respect to the energy [38].

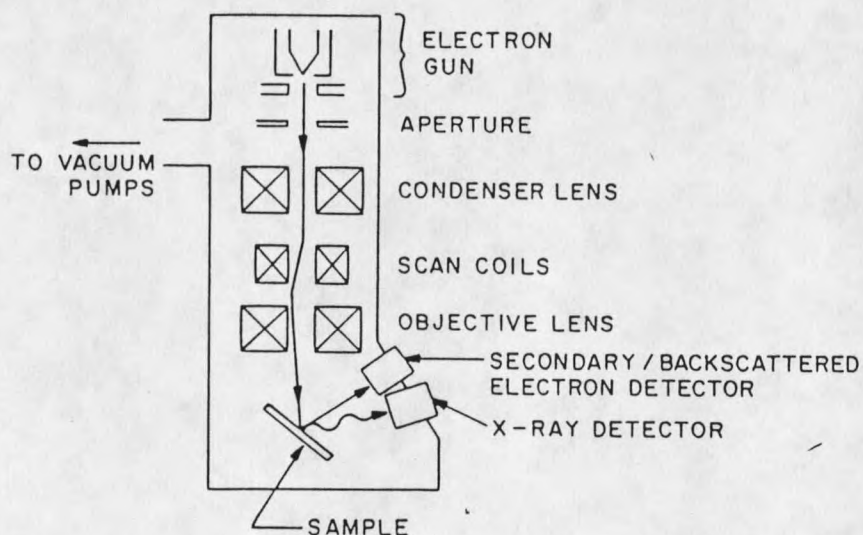


Figure 10. Schematic drawing of a scanning electron microscope [39].

- (1) Higher energy electrons. These electrons are backscattered and their energy is close to that of the primary beam.
- (2) Auger electrons. Peaks of these electrons occur between E_0 and 50 eV and they are discussed in detail in the Auger electron spectroscopy section.
- (3) Lower energy electrons. They generally have energies between 0 eV and 50 eV, peaking at less than 5 eV. These electrons are referred to as secondary electrons and are produced by inelastic collisions of the primary beam and the inner shell electrons of the sample atoms.

Because of their low energies, the only emitted secondary electrons are those which suffer the least inelastic scattering, and thus come from the atoms located very close to the surface. The escape depth of electrons in metals reaches a minimum of 4 Å at 70 eV, and increases with decreasing energy to a value of 25 Å at 10 eV. The escape depth is more than 50 Å for insulators. Because secondary electrons have a short escape depth, they exhibit better point-to-point resolution than do backscattered electrons. Mostly, secondary electron current rather than backscattered current is used to modulate the intensity of an electron beam in a cathode ray tube (CRT). The rastering incident beam of the SEM and the CRT

electron beam move synchronously across the sample surface to produce the image on the CRT screen.

A schematic diagram of an SEM is shown in Figure 10. The electron beam source can be tungsten hairpin, lanthanum hexaboride (LaB_6), field emission, and Schottky emitter sources which give different resolution and brightness levels.

The contrast of the image depends on the variations in the flux of electrons arriving at the detector [40]. Secondary electron yield is a strong function of the work function of the material, and is significantly higher for oxides and other wide-band gap materials than for silicon. The second source of contrast in secondary electron images is due to the dependence of secondary electron yield on surface curvature. The electron flux from a surface of changing slope varies with the secant of the tilt angle, thus making surfaces with different slopes easily distinguishable. The last source of the contrast is the orientation of the emitting surfaces with respect to the detector. Surface regions that face the detector appear brighter than other surface regions.

Auger Electron Spectroscopy

Auger electron spectroscopy (AES) is a quite commonly used electron spectroscopic technique [41,42]. The Auger electron emission process for silicon is shown in Figure 11 [43]. When an electron or photon strikes the surface of the sample, a primary electron is ejected from the K-shell of the

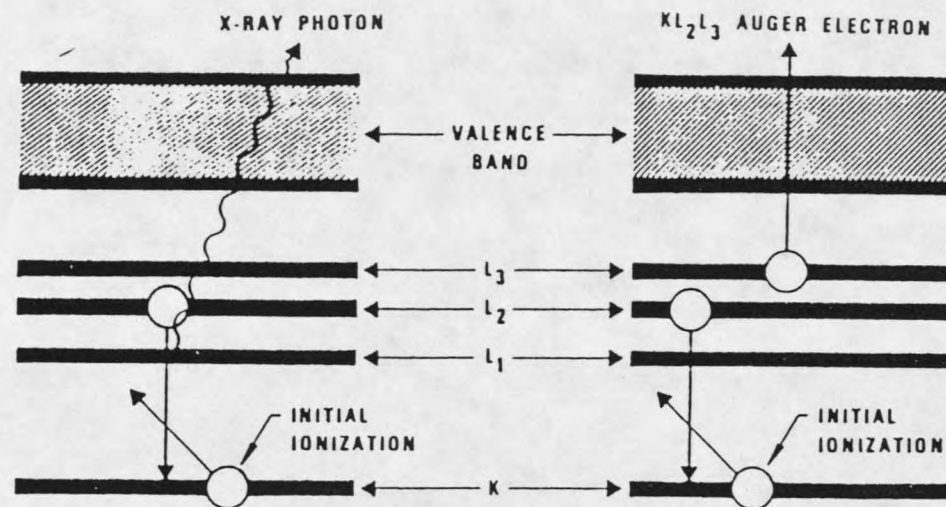


Figure 11. X-ray and Auger electron emission during de-excitation of atom after initial ionization [43].

atom leaving a hole in the core level of the system. An electron from the L-2 level relaxes into the K-shell to fill the empty position. During the relaxation process, a photon is emitted. This photon may either escape the material or interact with it. In the case of interaction it causes the ejection of a lower energy electron, such as L-3 level. This ejected electron is called an Auger electron and is labelled a KLL Auger electron in this case. Auger electrons are characteristic of the atom that emitted them. Since the Auger process requires the involvement of three electrons, H and He can not be detected with AES.

The incident electron beam energy is generally around 2-10 keV and can penetrate only a short distance into the sample. Most Auger electron energies are between 20 and 2,000 eV. Electron escape depth is defined as the distance from the surface across which the number of monoenergetic electrons emitted drops to 36.8% (e^{-1}) of their original value. The escape depth for Auger electrons is generally less than 50 Å. This enables one to perform a chemical analysis of surface regions from AES data.

It is shown in Figure 9a that Auger electrons constitute a small portion of the number of electrons emitted from a surface, therefore noise from other types of electrons is inevitable. Auger electron signals can be distinguished by performing a differentiation (dN/dE) using lock-in amplifiers

as shown in Figure 9b. An Auger spectrum of a W film surface on Si is given in Figure 12.

AES can detect elements above the concentration range of 0.1-1% at the sample surface. Quantitative information about the composition C_i of element i is obtained from the formula

$$C_i = \frac{\alpha_i I_i}{\sum \alpha_j I_j} \quad (16)$$

where, I_i is the intensity of the Auger peak of pure element i , and j indicates a summation over all the elements present in the matrix. The proportionality constant α is determined from known standards.

It is also possible to obtain compositional information about the material beyond the escape depth of Auger electrons. To achieve this, AES is combined with ion sputtering. During the AES analysis, ion sputtering is used for the continual creation of new surfaces through the sample. Data are then obtained by interrupting the sputtering at regular intervals and taking an Auger spectra. Hence, one can plot Auger peak heights as a function of sputtering time (or the equivalent depth) to obtain an AES depth profile. The incident electron beam size mostly determines the lateral resolution and is smaller than $0.1 \mu\text{m}$. Auger electron escape depth, on the other hand, determines the depth resolution and is about one monolayer for lower energy electrons.

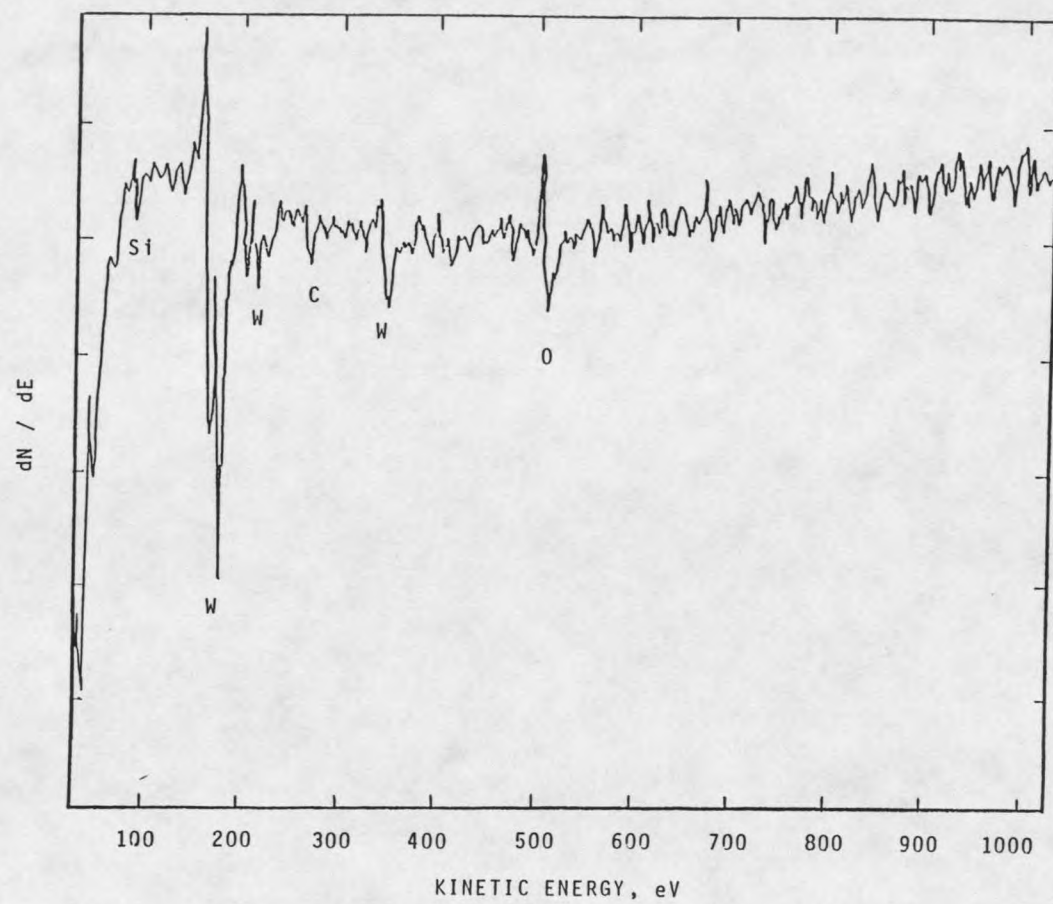


Figure 12. Auger spectrum of W film surface on Si.

Other important characteristics of AES are as follows: Upon exposure to an electron beam, samples of non-conducting nature have a propensity to charging. Thus, the analysis of insulators by AES is limited. A high energy incident electron beam can damage the surface under examination. Ion sputtering during depth profiling is a destructive method. Matrix effects can alter the signal position and intensity. Larger detection areas, longer scan times and narrower energy range scans increase the detection limit.

The common application of AES to VLSI technology includes the analysis of dopant and contaminant concentration in thin films and on surfaces, and determination of interface characteristics [43].

Film Thickness Measurement

Thickness of the deposited thin films is crucial in VLSI applications [44]. A thinner film introduces a higher resistance which can result in poor device performance. On the other hand, a thicker film will require longer etching times to reach the desired film thickness necessary for the application. Mostly, the thickness during physical evaporation is monitored with a resonator plate made from a quartz crystal. In the case of chemical vapor deposition, the reactive nature of the gases involved makes it necessary to use post-deposition measurement techniques. After deposition, measurement of metal film thickness can be performed directly

with a stylus profilometer or SEM cross-sectional views of the films. Indirect measurement methods include electrical measurement of sheet resistivity and employment of gravimetric methods.

In the case of surface profiling, a fine diamond stylus is drawn over the substrate surface [44,45]. In the measurement process, the stylus encounters a step where the film has been masked during deposition or etched after deposition. The height of the step is then detected by the variation in signal based on differential capacitance or inductance techniques. Films less than 1000 Å can be measured with this technique with an accuracy better than 100 Å.

Cross-sectional scanning electron microscopy (SEM) pictures are commonly used to analyze deposited film thickness as well as morphology. The Si wafers are scribed on the back side and fractured. The SEM image is taken along the fractured surface until a good view of deposited film-substrate interface is found. Actual film thickness is determined from the magnification level. A reasonable difference in the brightness level, thereby the work functions, of substrate and film is essential in this technique.

The sheet resistance measurement technique is explained in detail in section "Sheet Resistance". This method assumes that deposited metal has the same resistivity as the bulk metal that also includes the same porosity, crystal structure,

and composition [46]. Films thinner than about 1000 Å are normally measured with this technique.

The gravimetric method is simply to weigh the substrate before and after film deposition by using a microbalance [44]. If the film is assumed to have a bulk density of ρ_b , the thickness is found by

$$\delta = \frac{\Delta m}{\rho_b A} \quad (17)$$

where, Δm is the increase in mass and A is the area. Note that Δm can also be obtained by etching the deposited samples. This method is explained in the experimental section.

Chemical Vapor Deposition

Chemical vapor deposition (CVD) is the deposition of non-volatile solid film on a substrate by chemical reaction of gaseous reactants [47]. The reactants enter the reaction chamber in gaseous form and react upon reaching the hot substrate surface to form the film. Many refractory materials such as metals, metalloids, oxides, carbides, borides, nitrides, silicides, and sulfides can be deposited by chemical reaction of gaseous reactants. One can use the CVD process to deposit essentially amorphous or microcrystalline materials as well as two- or three-dimensionally large single-crystalline materials.

VLSI fabrication technology utilizes CVD in a variety of areas such as the epitaxial growth of single-crystal silicon films, and the deposition of amorphous and polycrystalline thin films. CVD of refractory metals and their silicides is of special interest for the metallization process.

CVD metals formed by hydrogen reduction of metal halides are of importance for two reasons [48]:

- (1) The randomly oriented fine-grained material is useful for many structural shapes and the convenience of vapor forming makes it economical.
- (2) Preferentially oriented metal (especially W) has a uniform electron or ion emission property.

In summary, CVD processes offer a number of advantages over other deposition processes [47]. These advantages are:

- (a) It is possible to deposit high purity films.
- (b) Films with a wider range of chemical compositions can be attained.
- (c) CVD delivers the required film properties for some materials where other methods are inadequate.
- (d) For many films, the CVD process is economical and easier to control.

Applications of CVD films in VLSI technology include a variety of basic insulators, semiconducting layers, conducting layers, and superconducting films. Among the most commonly used films are silicon dioxide (SiO_2), silicon nitride (Si_3N_4), and polysilicon (Si). CVD films are expected to meet requirements for both the efficiency of the manufacturing steps and the final device performance.

Basic Steps in CVD

A CVD process basically is a type of surface catalysis process since the deposition process is thermodynamically favorable and takes place on the substrate surface. Most of the time the surface serves as a catalyst for the reactions leading to deposition and crystal growth. The same sequence of events in a heterogeneous reaction can therefore be applied to crystal growth by CVD [47,49]. These events are:

- 1) Introduction of reactant gases and diluent inert gases into the reaction chamber.
- 2) Transport of reactants to the substrate surface.
- 3) Adsorption of reactants on the surface.
- 4) Surface processes such as surface diffusion of adatoms, chemical reaction, and site incorporation.
- 5) Desorption of gaseous by-products.
- 6) Transport of gaseous by-products to the main gas stream.
- 7) Removal of by-products from the reaction chamber.

Experimental Parameters in CVD

Any one of the several steps taking place in a CVD process can be the rate-determining step. A number of experimental parameters play an important role in determining or altering the rate-determining step. The experimental parameters, which are discussed individually below are: deposition temperature, gas flow rate, crystallographic orientation, substrate position, reactant partial pressure, and surface area.

Deposition Temperature: Surface-reaction rate expressions can be written as a product of temperature- and pressure-dependent terms as

$$\text{Rate} = f_1(\text{Temperature}) f_2(\text{Composition}) \quad (18)$$

The temperature-dependent term is usually expressed by the Arrhenius equation

$$R = R_0 e^{(-E_a/kT)} \quad (19)$$

where, R is the rate constant at temperature T , R_0 is the frequency factor, k is the Boltzmann constant, and E_a is the activation energy for the process. Activation energy signifies the presence of an energy barrier which must be overcome in order for the process to occur. Adsorption, desorption, surface reaction, and surface diffusion can be described in this way as they involve activated reactions with the surface.

Activation energies for most surface processes are usually greater than 10 kcal/mole (0.43 eV/atom) and lie in the range of 25-100 kcal/mole (1.08-4.34 eV/atom) [49]. Exceptions to this generalization are reported in the literature [50].

Conversely, mass transport phenomena such as diffusion are almost insensitive to temperature. The temperature dependence of diffusion coefficients for molecular species is given as T^m , where m is between 1.5 and 2 [49]. Such a dependence yields small values (3-8 kcal/mole or 0.13-0.35 eV/atom) when plotted as an Arrhenius expression to find activation energies. Therefore, a preliminary distinction between the surface phenomena and the gas phase mass

transport phenomena can be made by observing the temperature dependence of the process.

An Arrhenius plot is a semilogarithmic plot of the rate constant (or rate for a fixed flow rate - or concentration - of reactants) versus reciprocal of the temperature. At lower temperatures, a classical Arrhenius plot exhibits a straight line which has a slope proportional to the activation energy of the surface reaction as shown in Figure 13. In this region, there is always enough supply of reactants to the surface and this supply is faster than the consumption of the reactants during the reaction. Then the overall rate is controlled by the surface kinetics. As the temperature is increased, the increase in surface reaction rate reaches such a level that the rate of mass transfer of reactants from the bulk to the surface becomes insufficient. A further increase in the temperature does not significantly increase the reaction rate because the rate is limited by the rate at which reactants are supplied to the surface. Then it is said that mass transfer is the rate-controlling mechanism. However, one should be very careful in stating a mass-transfer limited regime without corroborating evidence, for the Arrhenius plot gives the same behavior when there is not enough supply of reactants to the reactor, or when the reactant desorption rate becomes larger than the adsorption rate [51].

Thermodynamic aspects of the reaction system should also be considered when examining an Arrhenius plot. It is known

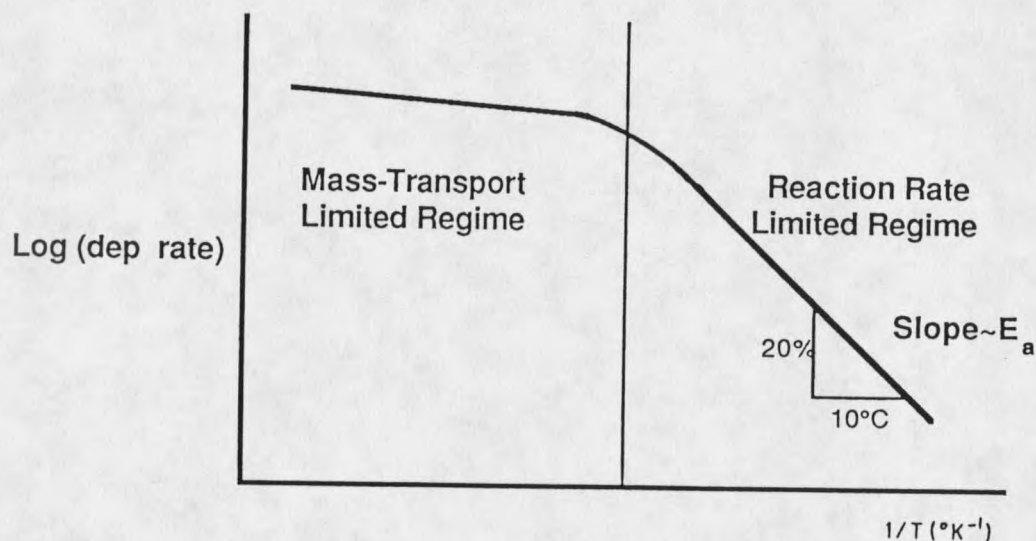


Figure 13. Temperature dependence of growth rate for CVD films [47].

that equilibrium processes exhibit rate-temperature variations which can be predicted from thermodynamic data [49].

Figure 14 illustrates the variation of rate with reciprocal temperature for different values of the heat of reaction; zero in curve B and negative in curve A (exothermic). At high temperatures, curve B approaches a slope where the rate is proportional to $T^{1.5}$, indicating a mass transport control. However, in curve A the rate decreases at temperatures higher than $\sim 750^\circ\text{C}$, indicating a thermodynamic limitation.

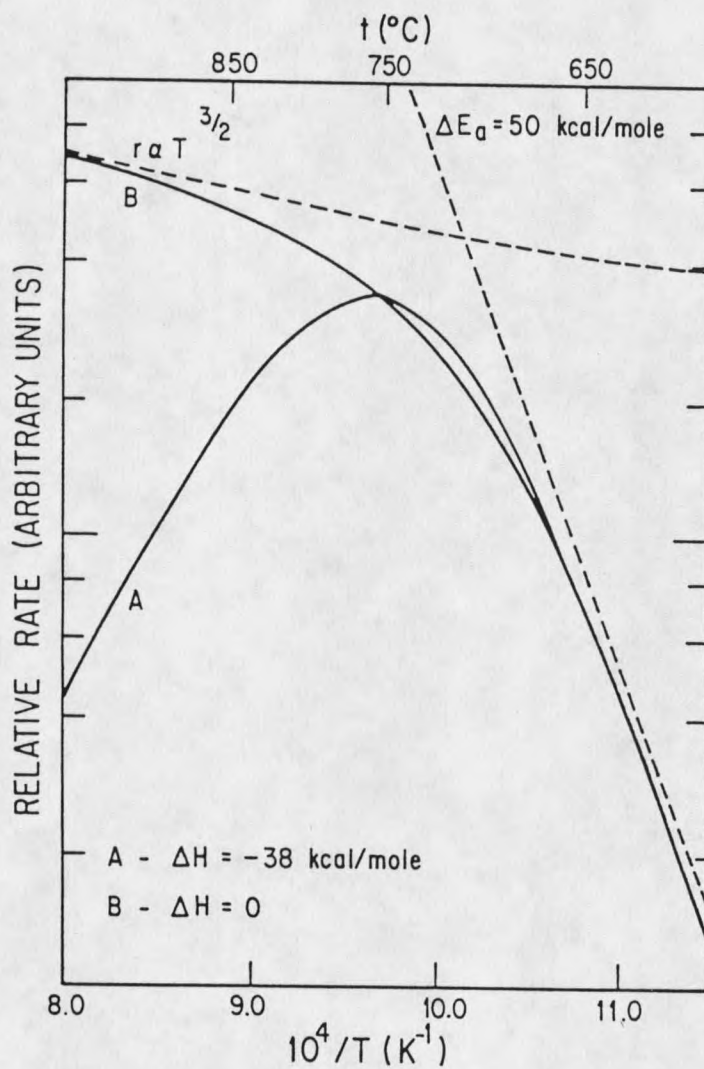


Figure 14. Reaction rate as a function of reciprocal temperature for zero and negative heat of reaction [49].

Figure 15 shows how the Arrhenius plot could change with changing positive values of the heat of reaction (endothermic). The increase of rate with temperature, in this case, is determined by the thermodynamics of the process rather than by the kinetics. Therefore, a high apparent activation energy does not necessarily indicate control by reaction kinetics.

Concentration dependence of the heat of sorption may also contribute to the activation energy. The procedure to find the true activation energies for this case is given in the literature [52]. Nevertheless, high activation energies strongly support kinetic control for exothermic processes [49].

Gas Flow Rate: When a linear growth rate for a CVD process is plotted as a function of reactant gas flow rate, the generalized form of the relationship is shown in Figure 16 [53]. At very small flow rates (Region I), the incoming gas stream has sufficient residence time to equilibrate with the substrate surface. Increasing the total flow rate increases the rate of reactant input, and thus more material per unit time equilibrates with the substrate surface. The rate increases linearly with total flow rate in this region [54].

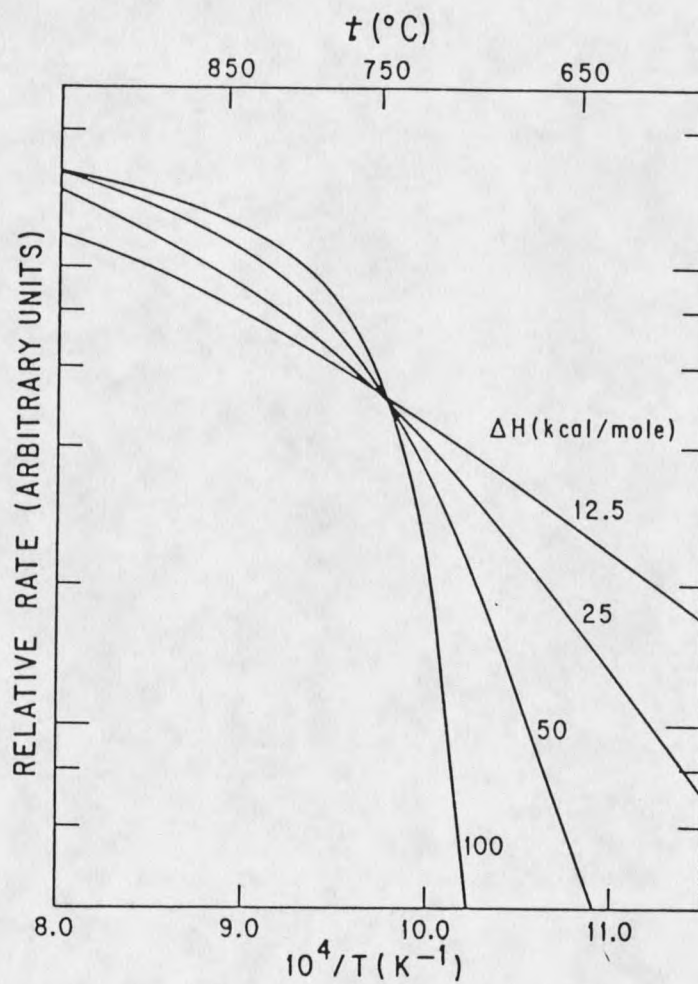


Figure 15. Reaction rate as a function of the reciprocal temperature for positive heat of reaction, illustrating erroneous apparent activation energies [49].

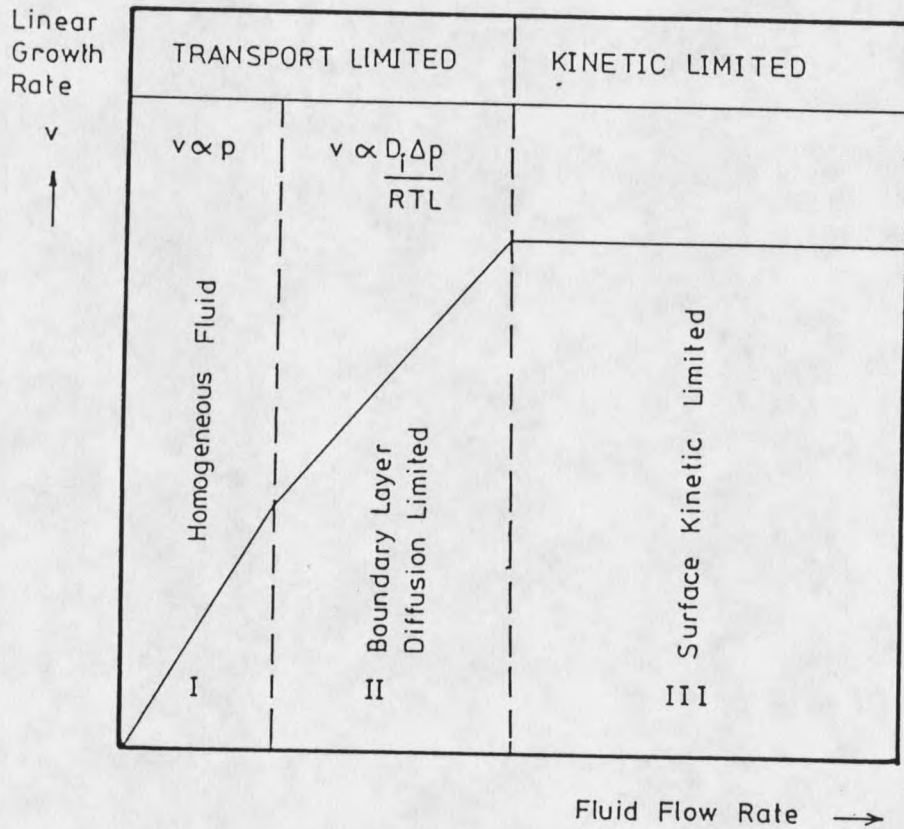


Figure 16. Idealized growth-rate versus fluid flow-rate plot showing the different growth regimes [53].

When the flow rate is increased above a certain point, the entire gas stream no longer has sufficient residence time for complete equilibration (Region II). At this point a portion of the incoming reactants pass by unreacted. This gives higher bulk stream partial pressures than the surface partial pressure. Then the rate-limiting process is diffusion from the main gas stream to the substrate surface. It is known that the boundary layer thickness, where the diffusion process takes place, is inversely proportional to the square root of the gas velocity [55,56]. Then, in this regime, the surface reaction shows a square root dependence on the gas flow rate.

At high flow rates, the reaction rate reaches a plateau (Region III) and becomes independent of flow rate [56]. Here the reaction rates are so slow relative to the gas flow and mass transfer rates that the partial pressure at the surface becomes essentially the input partial pressure. Then the process is said to be "kinetically controlled". The reactant flow rate for kinetic studies should be in this plateau regime so that the true temperature and partial pressure dependence of the reaction can be observed.

Crystallographic Orientation: Adsorption, desorption, and surface reaction are surface phenomena which involve surfaces chemically or take place on them. Different crystal orientations of a surface display different atomic arrangements and densities. As a result, the nature of the

surface has an effect on the rates of surface processes. For example, for GaAs deposition with surface kinetics controlling, the {111}A orientation has grown 16 times faster than {111}B orientation [57]. These two orientations have the same atomic density and geometry. The only difference is that one is terminated in a layer of Ga atoms and the other in a layer of As atoms. Effects resulting from the chemical differences of these two are called polarity effects. The relative rates of polar orientations can be altered considerably by changing the vapor concentrations or reactant ratios [58,59]. Surface diffusion rates are also reported to depend on crystallographic orientation [60].

Substrate Position: A change in substrate position may alter the flow patterns in the reactor which in turn influence the boundary layer thickness development and reactant distribution across the substrate surface. In principle, kinetically limited processes are independent of flow pattern changes. Mass transport (diffusion) controlled processes, however, are susceptible to changes in the flow dynamics [49]. Thickness uniformity of the deposited film can be significantly changed by altering the substrate position. Therefore, rate variations with substrate position offer support for diffusion control.

Reactant Partial Pressure: For simple processes, both diffusion and kinetic steps are first order in the reactant partial pressure. Therefore, first order dependence cannot be used to evaluate the rate limitations [49]. The dependence of reaction rate on reactant partial pressure can be used to characterize the reaction mechanism when the process is kinetically controlled. A basic error found in the CVD literature, including the $\text{SiH}_4\text{-WF}_6$ system, is that partial pressure dependence of some reaction systems have been reported while the reaction systems are shown to be mass-transport limited [49].

Surface Area: A surface reaction rate constant is a function of the actual surface area [49]. Initial substrate surface roughness or porosity developed in the depositing film will increase the actual surface area for reaction and give higher rates.

Chemical Vapor Deposition Reactors

Chemical vapor deposition reactor design depends on operating conditions of the deposition process and can be categorized according to two basic criteria [12,47]:

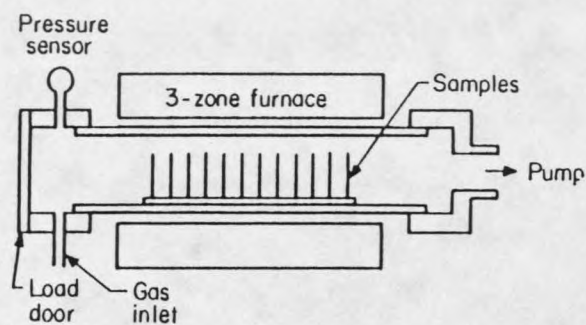
(1) Depending on the method used to heat the wafers, it can be either a hot-wall or a cold-wall reactor. (2) Operation pressure regime is also used in grouping terminology such as atmospheric pressure or reduced pressure reactors (Figure 17).

Heating methods for wafers are resistance heating, rf induction heating, energy from a glow discharge (plasma), and photons.

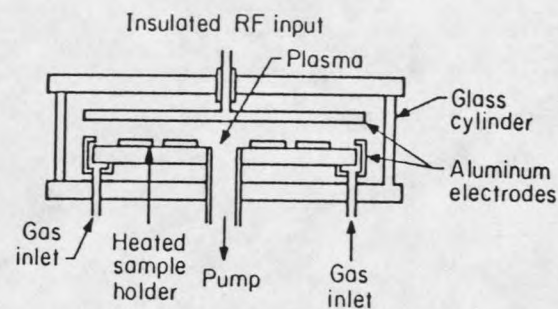
Hot-wall Reactors: A hot-wall reactor is essentially a quartz tube heated by resistance-heating coils surrounding the reaction tube. In this way, not only the wafer but also the reactor walls are hot, and that results in deposition on the interior walls. This, in turn, may cause reactant depletion on the wafers. Wafers stand vertically, perpendicular to the gas flow, in a quartz holder. Hot-wall reactors allow good throughput, large wafer diameters and good film uniformity. The disadvantages are the requirement of frequent cleaning, relatively low deposition rates due to reduced pressures and frequent use of toxic, corrosive or flammable gases [61].

Cold-wall Reactors: When the heating is done via rf induction or infrared lamps mounted in the reactor, it stays restricted to the wafers and susceptor [47]. In this case, the reactor walls essentially stay cold and the reactor is called a cold-wall reactor.

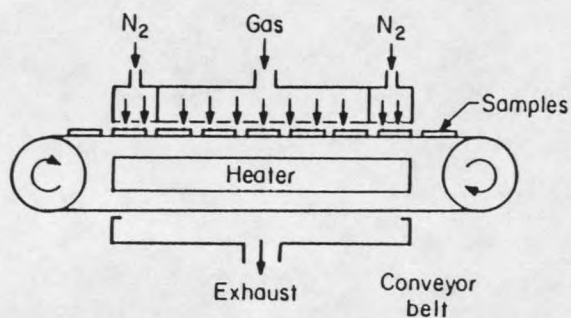
Atmospheric Pressure Reactors: Atmospheric pressure chemical vapor deposition (APCVD) reactors are easier to design and they provide relatively high deposition rates [62]. Operation is in the mass-transport limited regime. This limits



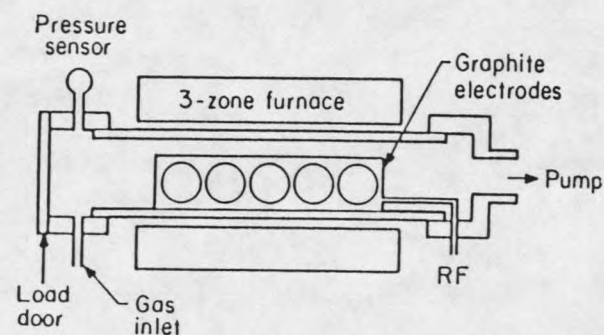
(a)



(c)



(b)



(d)

Figure 17. Schematic diagrams of CVD reactors. (a) Hot-wall, reduced-pressure reactor. (b) Continuous, atmospheric-pressure reactor. (c) Parallel-plate. (d) Hot-wall. [12]

the flexibility in reactor geometry as it is necessary to supply reactants on the substrates uniformly throughout the reactor. APCVD reactors are used for low-temperature oxide (LTO) deposition and epitaxy [47].

Horizontal tube APCVD reactors are hot wall reactors and are used very little in VLSI processing. Their disadvantages are low throughput, poor thickness uniformity, and particulate contamination.

Continuous processing APCVD reactors can provide better thickness uniformity, low contamination, and high throughputs. In the process, the wafers are moved at a constant speed through the heated section by means of a plate or a conveyor belt. Reactant gases flowing through the reaction zone are isolated from outside air by curtains of flowing gas. These reactors require very fast gas flows and need frequent cleaning.

Low-pressure CVD Reactors: Low-pressure chemical vapor deposition (LPCVD) reactors operate at medium vacuum (30-250 Pa or 0.25-2.0 Torr). Reduced pressure increases the gas phase diffusivity and reduces the mass-transfer restrictions for the deposition reaction. Therefore, LPCVD reactors operate more in the reaction-rate limited regime. Elimination of mass-transfer limitations provides high wafer capacity, better thickness uniformity and less gas phase reactions (i.e. less particulate contamination) [63]. The disadvantages are the low deposition

rates and the relatively high operation temperatures. There are two main design configurations of LPCVD reactors, horizontal tube and vertical flow isothermal.

Horizontal tube LPCVD reactors are hot-wall reactors and are widely used for depositing poly-Si, silicon nitride, and undoped and doped SiO_2 films [47]. They are superior in terms of economy, throughput, uniformity, and ability to accommodate large diameter wafers. However, they provide low deposition rates and still are susceptible to particulate contamination [61]. As mentioned earlier, LPCVD reactors operate in the reaction-rate limited regime, therefore equal mass transport to all parts of every wafer is not critical. Wafers are therefore stacked vertically at very close spacing. Compared to APCVD, the gain by a larger number of wafers being processed far outweighs the loss by lower deposition rates; the net result is a higher throughput for the LPCVD reactor. Reactants are fed from one end of the tube and are pumped out from the other end. Depletion effects are still observed towards the end of the tube as reactant concentration decreases. This can be compensated either by linearly increasing temperature in the direction of flow or by introducing the reactants at several points along the tube length. The latter arrangement is known as distributed feed.

A vertical-flow isothermal LPCVD reactor is the improved form of the distributed gas feed technique on a cold-wall reactor [64]. Wafers are stacked in perforated quartz cages.

and the gases are introduced through the perforations. In this way, identical quantities of fresh reactants are supplied to each wafer. This design allows highly uniform depositions with low particulate contamination.

Plasma-enhanced CVD Reactors: The method of energy input for the deposition reaction is also used in the grouping terminology for CVD reactors. Plasma enhanced CVD (PECVD) reactors utilize plasma (glow discharge) created by an rf induction onto a low pressure gas [47]. Since the reactant gases are more reactive in the plasma state than the neutral state, PECVD is carried out at substrate temperatures lower than those of APCVD and LPCVD process. The radicals formed in the plasma discharge have high sticking coefficients and upon adsorption they can migrate easily on the surface to yield conformal structures. Films with low pinhole density and with good adhesion to the substrate can be deposited with this method. PECVD reactors are widely used for the deposition of silicon nitride and SiO_2 over metals. PECVD films are not stoichiometric because of the complexity of the reaction and are contaminated with by-products and incidental species. These contaminants cause problems in later stages of manufacturing MOS circuits. When compared to an LPCVD process, the PECVD process is dependent on additional parameters such as rf power density, frequency, and duty cycle.

There are three basic types of PECVD reactors: (1) the parallel plate type, (2) the horizontal tube type, and (3) the single wafer type.

Photon-induced CVD Reactors: Photon-induced chemical vapor deposition (PHCVD) uses high-energy, high-intensity photons either to excite the reactant gases or to heat the substrate surface [47]. Good step-coverages at low temperatures are possible with this method but contamination of films is the main disadvantage. A UV lamp or laser is used as energy source [65]. Extremely low deposition rates make PHCVD reactors infeasible for the microelectronic industry.

Chemical Vapor Deposition of Tungsten

It was in the early 70's that polysilicon technology started to be widely employed in the fabrication of metal-oxide semiconductor (MOS) VLSI circuits. The advantages were compatibility with silicon wafer processing, the capability of self-aligning features, stable and controllable gate electrode characteristics, applicability of simple deposition techniques such as CVD, and narrow linewidths readily patterned with selective dry etching processes [66].

Figure 18 shows address access times for polysilicon and refractory metal gates as a function of gate length [67]. For a polysilicon gate, decreasing gate lengths down to 2 μm gives decreasing gate address access time, which results in shorter signal processing time. However, below 2 μm , access time increases with decreasing gate lengths. Here at very small dimensions, the high resistivity of polysilicon (20 ohm/square sheet resistance) projects the impact of RC delay time on circuit performance. RC delays are defined as delays caused by resistance and capacitance of interconnect lines. On the other hand, a refractory metal silicide gate (1 ohm/square sheet resistance) gives smaller access times with decreasing gate lengths even below 2 μm . This limitation of polysilicon forced researchers to explore the employment of refractory metals such as tungsten (W) and molybdenum (Mo) as gate electrodes and interconnections in metal-oxide semiconductor field-effect

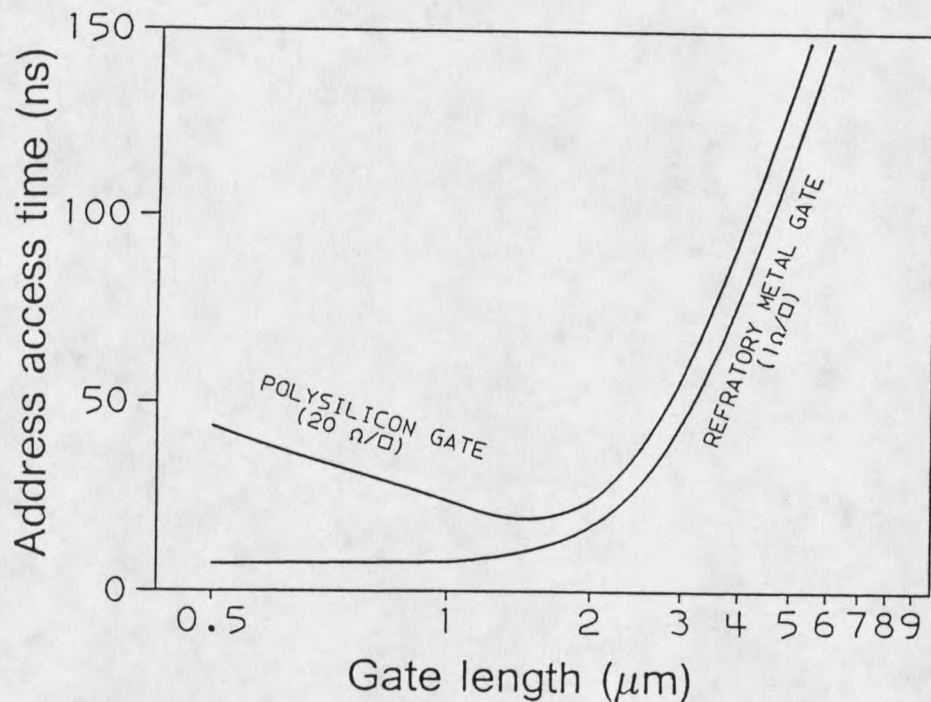


Figure 18. Address access time as a function of gate length. For geometries below $2\mu\text{m}$, access time for 4K static NMOS RAMs are improved by using refractory metal gates [67].

transistor (MOSFET) technology. Starting from late 1960's the feasibility of refractory silicides as a replacement for polysilicon was explored [68-70]. In 1983, VLSI technology utilized polycides deposition by co-sputtering of molybdenum or titanium silicide [66]. (The term polycide is used for a multilayer structure, consisting of a low resistance material, such as refractory metal silicide, on top of a doped polysilicon layer.) However, the technical difficulties

associated with co-evaporation techniques directed manufacturers to switch to the LPCVD process. In 1986, the first volume production of 1 M DRAM used tungsten silicide deposition by LPCVD.

As ultra-large scale integration (ULSI) is becoming a reality, the dimensions are decreasing to sub-micron levels. Silicide films at these thickness levels cannot produce a low enough sheet resistance to meet the demands for device performance. Thus, a lower resistivity advantage of metals over metal silicides makes metallized polysilicon and metallized source/drain regions attractive [71]. Selective metal deposition has been a special interest for its self-aligning, self-patterning capability [72].

CVD tungsten was accepted as an excellent interconnect material and applications at production level have already started. Tungsten provides low resistance ($5.6 \mu\Omega\text{-cm}$ of bulk resistivity), low stress ($<5 \times 10^9 \text{ dyn/cm}^2$), excellent conformal step coverage and a thermal expansion coefficient which is close to that of silicon. Another important feature for tungsten is its high resistance to electromigration, while in the current technology aluminum severely suffers from it. CVD tungsten films can also form low resistance contacts to silicon. Figure 19 gives the potential applications of CVD tungsten. The use of tungsten as interconnect metal improves the wirability in the circuit and hence reduces wiring delays. The incorporation of vertical vias into the structure improves

Table 1. Free Energy Changes at 600 K [7].

Reactions	ΔG , kcal/mol
1) $WF_6 + 1.5Si \rightarrow W + 1.5SiF_4$	-179.4
2) $WF_6 + 3H_2 \rightarrow W + 6HF$	-27.9
3) $WF_6 + 1.5SiH_4 \rightarrow W + 1.5SiF_4 + 3H_2$	-208.7
4) $WF_6 + 2.1SiH_4 \rightarrow 0.2W_5Si_3 + 1.5SiF_4 + 4.2H_2$	-227.6
5) $WF_6 + 3.5SiH_4 \rightarrow WSi_2 + 1.5SiF_4 + 7H_2$	-268.9

changes, ΔG , for WF_6 reactions at 600 K are given in Table 1 [7].

The Si reduction reaction yields tungsten films by consuming the exposed Si substrate. The reaction stops after a certain W film thickness is reached; this characteristic is called self-limiting. Once the limiting thickness is reached, the W film forms a diffusion barrier between the Si and WF_6 , and prevents further reaction. Films thicker than the limiting thickness can be deposited with the H_2 reduction reaction. Selective deposition of tungsten is also possible with both Si and H_2 reduction provided that certain temperature, pressure and flow conditions are met. When the H_2 reduction reaction is carried out, it is the Si reduction reaction that takes place first. The reason is that the negative free energy change for the WF_6 -Si reaction (-179.4 kcal/mol) is much larger than that for the WF_6 - H_2 reaction

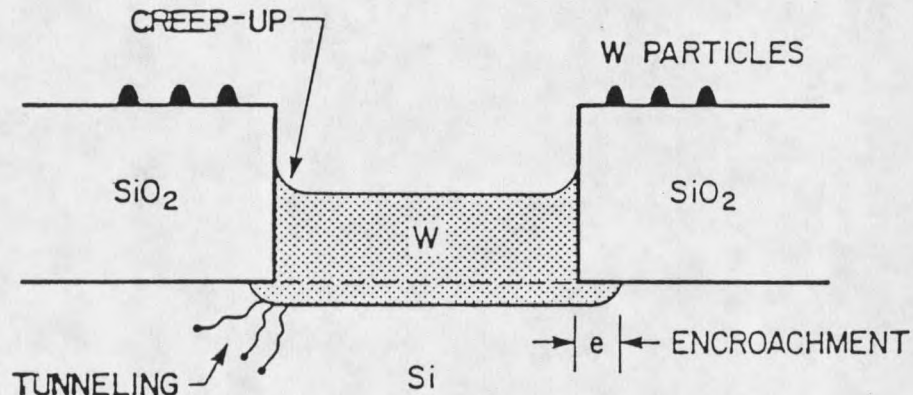
(-27.9 kcal/mol). This implies that the Si reaction can only be suppressed after the Si surface is coated with W by the Si-WF₆ reaction. Thus, the W/Si interface morphology is dictated by the Si reduction reaction. Since the Si reduction results in Si consumption, the junction may be damaged or broken. Figure 20 illustrates the common problems associated with selective W deposition by LPCVD. The problems such as encroachment, tunneling, creep-up, and loss of selectivity may either degrade the device quality or cause a complete failure.

The SiH₄ reduction reaction ($\Delta G = -208.7$ kcal/mole) is more favorable than the Si and H₂ reduction reactions. This reaction can suppress the Si reduction reaction and Si consumption. Higher deposition rates at relatively lower temperatures and smoother resulting W/Si interfaces make this reaction very attractive, especially for blanket W deposition. The problems such as tunneling and encroachment can be avoided with this reaction. Table 1 suggests that the SiH₄/WF₆ ratio should be kept below 1.5 to prevent any tungsten silicide (WSi_x) formation.

Background about each reduction reaction is given below.

Si Reduction of WF₆

There have been limited studies to evaluate the reaction mechanism of WF₆ by directly reacting with the silicon substrate. This reaction can be used to produce thin films of selectively deposited W. Most researchers observed a limiting



SELECTIVE LPCVD TUNGSTEN

Figure 20. Schematic illustration of several problems associated with selective W deposition by LPCVD [66].

deposit thickness, after which no further deposition took place. Morosanu and Soltuz [73] reported a linear dependence between tungsten growth rate and time; however, this behavior was not confirmed by others, as discussed later. Tungsten films were less than 10,000 Å thick and were deposited in an atmospheric CVD system.

Melliar-Smith, et al. [5] carried out the Si reduction of WF_6 in an inert atmosphere and found a limiting tungsten thickness of 300-400 Å in a temperature range of 420-880°C. In high flow atmospheric deposition conditions, Sauermann and

Wahl [74] have recorded limiting tungsten film thicknesses changing with deposition temperature. Limiting tungsten film thicknesses between 150 and 400 Å were also observed by Saraswat, et al. [75] and Moriya, et al. [76].

Busta and Wu [77] carried out experiments on single-crystal silicon wafers with native oxide thickness ranging from 3 to 60 Å. They were able to deposit 400-500 Å thick films on 12-15 Å thick native oxide layers. Above 40 Å thick native oxide, the W film thickness was practically zero. Tsao and Busta [78] observed a strong dependence of W film thickness on the precleaning procedure of silicon surfaces. They also recorded a decrease in thickness from 700 Å (maximum thickness) to 200 Å when the temperature was raised from 420°C to 500°C for polysilicon (440°C for single-crystal silicon). This decrease was explained as the etching of films by WF_6 which is catalyzed by the presence of phosphorus, present from doping. They proposed that the temperature dependence of the sticking coefficient of a reactive intermediate controls the reaction.

Broadbent and Ramiller [6] have spanned a pressure range of 0.1-5 torr and a temperature range of 300-425°C in their studies. They reported that a limiting tungsten thickness forms in as little as 0.1 min deposition time. At the beginning, the WF_6 -Si reaction occurs at a rate of at least 1000 Å/min until a limiting thickness of 100-150 Å is reached. Recorded tungsten film thicknesses were scattered within the

limiting values and under no conditions did they observe a linear dependence of film thickness on reaction time. The thickness was shown to be independent of the temperatures studied. Tungsten films were comprised of monocrystalline W grains. Nonuniformities in the thickness were attributed to the presence of a varying initial oxide layer on the Si substrate.

McConica and Krishnamani [79] have examined the silicon reduction of tungsten hexafluoride for a temperature range of 288-403°C and tungsten hexafluoride partial pressure range of 0.5-5 torr. The limiting thickness was between 100-400 Å and independent of time, temperature and WF_6 partial pressure. Electron spectroscopy for chemical analysis (ESCA) results showed oxygen in the films, which was believed to be the reason for the high resistivity. In every case the thickness was self-limiting. Similar to the findings of Broadbent and Ramiller [6], no linear dependence of film thickness on deposition time was observed.

Yu, et al. [80] have found that thermal annealing can cause the silicon atoms to diffuse through the tungsten film and segregate on the tungsten surface. Liftshitz [81] proposed that the formation of non-volatile lower fluorides of tungsten (where the most likely is tungsten tetrafluoride, WF_4) is responsible for the self-limiting effect. This hypothesis was supported by secondary ion mass spectroscopy (SIMS) results.

Raupp and Hindman [82] performed temperature programmed reaction (TPR) studies of WF_6 decomposition on Si(100) and W/Si(100) surfaces in ultra high vacuum (UHV) conditions. They observed that deposited tungsten rapidly chemisorbed WF_6 , and above 300K tungsten and silicon interdiffused. Clean bulk W readily dissociates and strongly adsorbs hydrogen; conversely, chemical vapor deposited tungsten (CVD-W) did not readily chemisorb hydrogen. Tungsten hexafluoride adsorbed less strongly on a native silicon dioxide surface, but was capable of partially reducing this thin oxide layer.

Green, et al. [83] examined the morphology of Si-reduced W films deposited between 210 and 700°C. The grains were spongy in structure, and the space occupied by trapped gases and pores was as high as 59%. Therefore, the film density was far less than tungsten bulk density.

Auger depth analysis showed that most of the oxygen in the W films is present at the Si/W [84]. Joshi, et al. [85] found 22-25% oxygen in the films deposited below 600°C, causing high film resistivities (130-140 $\mu\Omega\text{-cm}$). The oxygen level drops to 12-13% at higher temperatures resulting in lower resistivities (60-70 $\mu\Omega\text{-cm}$). A native oxide layer on the silicon surface was reported to be incorporated into the W films [78].

H₂ Reduction of WF₆

Tungsten can be selectively deposited on silicon, metal and silicide surfaces by the WF₆-H₂ reaction. SiO₂ and SiN₃ surfaces do not provide good nucleation sites for the deposition reaction. This property makes CVD tungsten by this reaction very attractive in integrated circuit manufacturing, because tungsten is deposited only on the desired surfaces. Selective deposition obviates the necessity for an additional masking, thus reducing the number of process steps and cost.

There have been quite a number of studies on the reduction mechanism of WF₆ in the presence of hydrogen. Holman and Huegel [86] obtained data regarding the effects of temperature, pressure, and vapor composition on the CVD reaction rate. Shroff and Delval [87] carried out tungsten and molybdenum deposition by the H₂ reduction of WF₆ and MoF₆ on copper, stainless steel and molybdenum surfaces. The H₂/WF₆ ratio was varied from 1 to 60 for a temperature and partial pressure range of 450-1200°C and 5-760 torr, respectively. For a constant H₂/WF₆ ratio, the deposition rate increased with total pressure, reached a maximum around 100 torr, then decreased. This maximum was observed to shift towards higher pressures as H₂/WF₆ ratio increased.

Cheung [3] interpreted the reaction as rate-limited by the activated adsorption of hydrogen. Further, H₂ dissociation is controlled by the jumping of one of the H atoms to a neighboring site. He also noted that HF desorption could be

rate-limiting under certain conditions. Bryant [4] stated that dissociation of H_2 molecules adsorbed on the substrate is the rate-limiting mechanism when gas phase diffusion limitations are absent.

Broadbent and Ramiller [6] examined the tungsten deposition rate as a function of substrate temperatures of 250-500°C and total pressures of 0.2-2 torr. The Arrhenius plots shown in Figure 21 exhibit a constant slope, signifying a congruent pattern of a rate-limiting reaction mechanism for the examined temperature and pressure range. The calculated activation energy of $E_a = 0.71$ eV/atom (69,000 J/mole) is very close to that previously reported as 0.69 eV/atom (67,000 J/mole) [3,4,86,88]. This is also the activation energy for surface diffusion of H_2 on W [89,90]. The tungsten growth rate shows a square root dependence on the total pressure ($R \propto P^{1/2}$) for constant H_2/WF_6 ratios. By keeping WF_6 partial pressure constant, the same square root dependence of the rate on hydrogen partial pressure ($R \propto P_{H_2}$) was also observed. The growth rate, however, was not dependent on the WF_6 partial pressure. These dependencies suggested that surface-adsorbed H_2 dissociation is the rate-controlling mechanism.

Another kinetic study performed by McConica and Krishnamari [79] used the same H_2/WF_6 ratio of 15 as did Broadbent and Ramiller [6]. The temperature and pressure ranges were 287-405°C and 0.2-10 torr, respectively. The activation

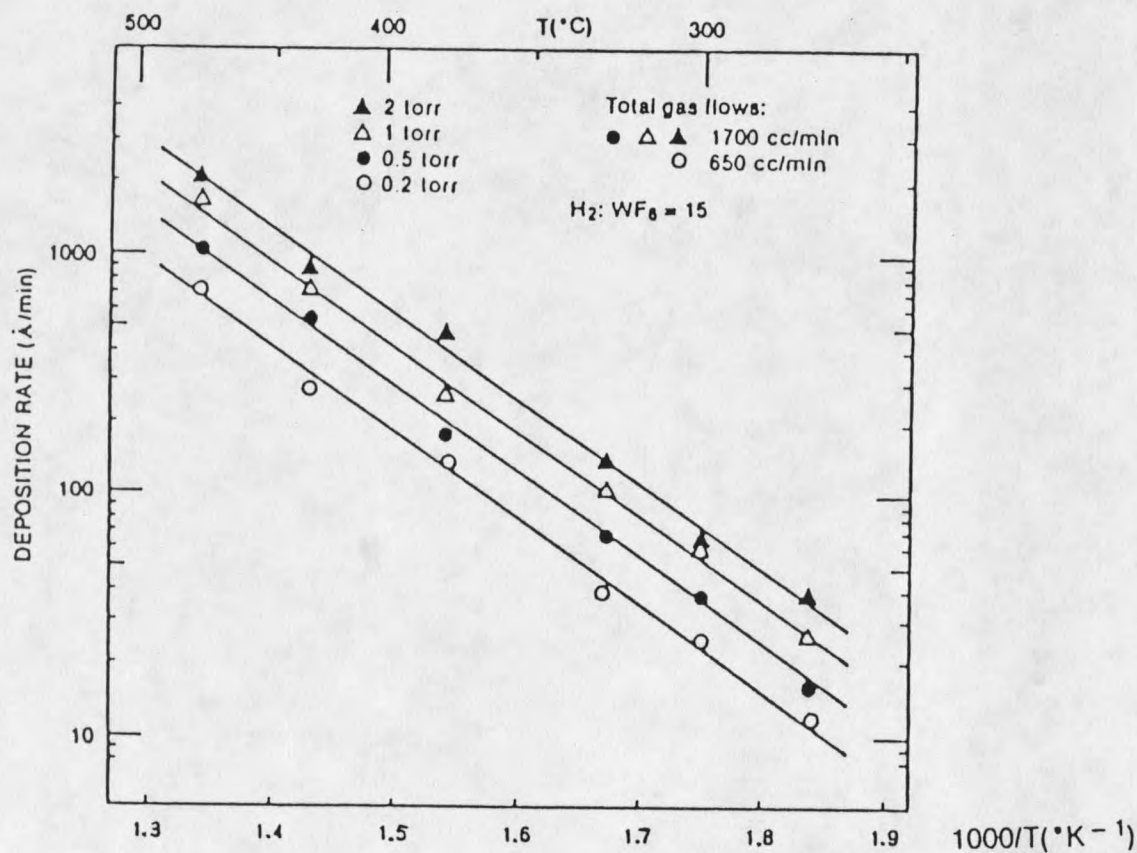


Figure 21. Arrhenius plot of deposition rate of CVD tungsten by H_2 reduction of WF_6 [6].

energy was reported as 0.76 eV/atom (73,000 J/moles), a higher value than previously reported. The growth rate was then expressed as

$$R = 6.8 \times 10^4 e^{(-8800/T)} (P_{WF_6})^0 (P_{H_2})^{0.5} \quad (16)$$

where, T is in K, P in Pa, and r in nm/s.

Selective deposition of W on Si surfaces constitutes another area of concern in the H₂-reduction reaction. Joshi, et al. [85] have found that the selectivity of tungsten produced by silicon reduction is almost 100% while that by H₂ reduction depends on the prior condition of the Si wafer. McConica and Krishnamani [79] observed that the selectivity loss to silicon surfaces occurs at temperatures higher than 300°C. The temperature dependence suggested that the tungsten nucleation on the oxide is an activated process. In a ultra high vacuum (UHV) analysis chamber, Creighton [91] performed Auger electron spectroscopy (AES) and temperature programmed desorption (TPD) studies on the selectivity loss. He suggested that a tungsten subfluoride desorption-disproportionation mechanism is the origin of transport of tungsten from the tungsten surface to the silicon dioxide surface. Tungsten pentafluoride, WF₅, was the best candidate to initiate the selectivity loss because of its volatility.

Studies of the CVD tungsten film morphology and impurity content are essential for the film quality, and thereby the film resistivity. Shroff and Delval [87] have measured the

fluorine content of W films with photon activation analysis. The deposition of low fluorine content films was possible at high temperatures, high H_2/WF_6 ratios and low pressures. Initial tungsten layers always started with a fine grain structure on the base metal substrates and continued to grow as elongated crystals. It was also reported that increasing H_2/WF_6 ratios and higher pressures resulted in less adherent and inhomogeneous coatings. This was exacerbated at high temperatures due to nucleation in the vapor phase.

Paine, et al. [92] observed wormhole formation in the Si substrate. They also reported W/Si interfacial roughness, and lateral encroachment. McLaury, et al. [93] have found that fluorine was a major contaminant in the films. Transmission electron microscopy (TEM) studies revealed damage at the (100) Si/SiO₂ interface in the form of worm tracks. Stacy, et al. [94] performed TEM analyses on the W films and confirmed tungsten deposition filaments (also called wormholes or tunnels) in the silicon substrate. Joshi, et al. [85] stated that H_2 reduction produces purer films than Si reduction by gettering oxygen in the reaction chamber. Thus, the resistivities for H_2 reduced films (9-10 $\mu\Omega$ -cm) are far less than those of Si reduced films (130-140 $\mu\Omega$ -cm). They also noted that hydrogen reduction produces very rough films compared to silicon reduction.

The frequently observed preferential tungsten crystal orientation in the H_2 reduction reaction is W(100) [87]. High

H_2/WF_6 ratios have been reported to give W(111) orientation [95]. In a more detailed structural study, Kamins, et al. [96] examined orientation change with thickness for W films. They used a chromium nucleation layer to prevent the Si- WF_6 reaction from influencing the W film structure. Figure 22 shows (100) dominance increasing with film thickness. The increase in (100) texture correlated with the increase in grain size, implying that (100) oriented grains grow at the expense of those with other orientations. Near the standard operating temperature of 300°C, the structure was not a sensitive function of temperature.

SiH₄ Reduction of WF₆

The employment of silane chemistry in W deposition reduces the need for process fine-tuning. A single-step deposition process eliminates silicon consumption which appears in the form of encroachment and wormholes. Silane chemistry substitutes for the initial silicon reduction step, since silane is more reactive than silicon in reducing tungsten hexafluoride. Thus, the silicon interface is not affected by direct tungsten deposition reaction and remains smooth. In spite of the recent extensive studies on the tungsten film quality and deposition parameters, the kinetics of the SiH₄- WF_6 reaction system has not been understood well and literature on the subject is very scarce.

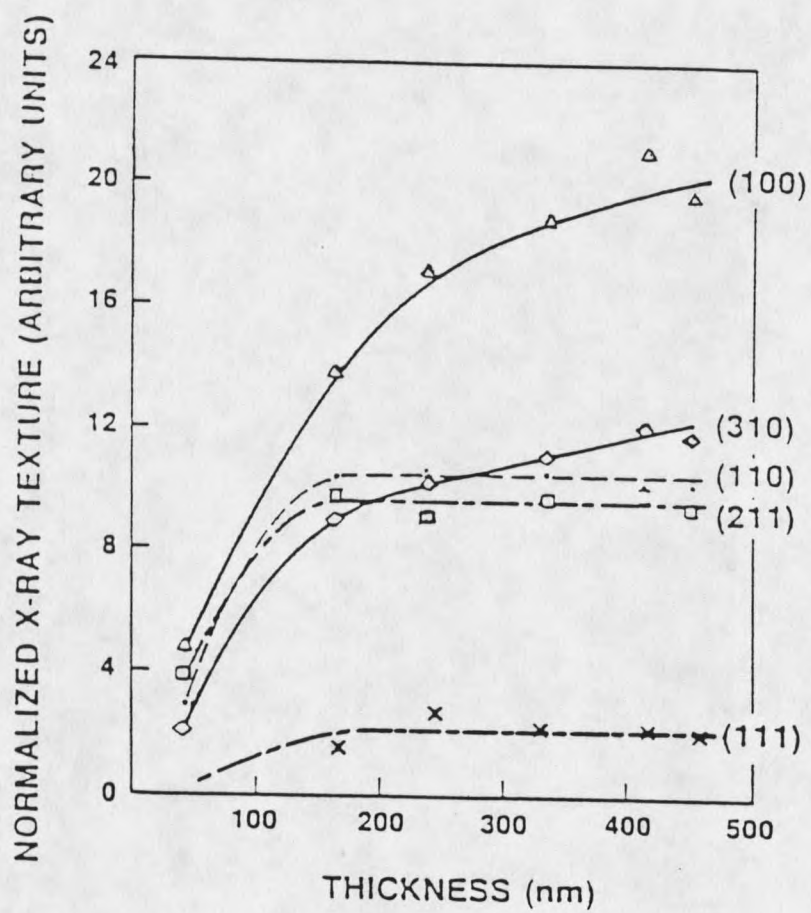


Figure 22. Normalized x-ray texture as a function of film thickness [96].

The first CVD literature on the SiH_4 - WF_6 system appears in 1973 by Lo, et al. [97]. Utilizing relatively higher pressures and temperatures ($P_{\text{total}} = 100$ torr, $T = 600$ - 800 °C) than is currently practiced in CVD-W process, they found that 1% Si in the films can break up the columnar structure of thick tungsten. The selective deposition of tungsten using WF_6 and SiH_4 was first examined in 1982 by Furuyama and Moriya [98]. They demonstrated that in a hot-wall system, much thicker W films can be grown using SiH_4 reduction instead of H_2 reduction. Several researchers have further studied SiH_4 reaction as an alternative to H_2 reduction of WF_6 [99-103].

Kusumoto, et al. [7] used TEM analysis to confirm that the tunnel formation can be eliminated when SiH_4 is used as the reducing agent in place of H_2 . The deposition was selective to Si when the SiH_4/WF_6 ratio was less than 1.5, and no tungsten silicide was formed until the ratio exceeded 2.1. The Arrhenius plots for the temperature range of 260-360 °C showed maxima, and the reason was speculated to be a change in the reaction mechanism (Figure 23). The deposition rate was not dependent on WF_6 partial pressure but on SiH_4 partial pressure. They noted that H_2 addition depresses the reaction since H_2 is a reaction product.

Ohba, et al. [8] studied the selective chemical vapor deposition of tungsten using silane and polysilane reduction of tungsten hexafluoride at a total pressure of 0.3 torr. At low temperatures, the reaction rate was up to three orders of

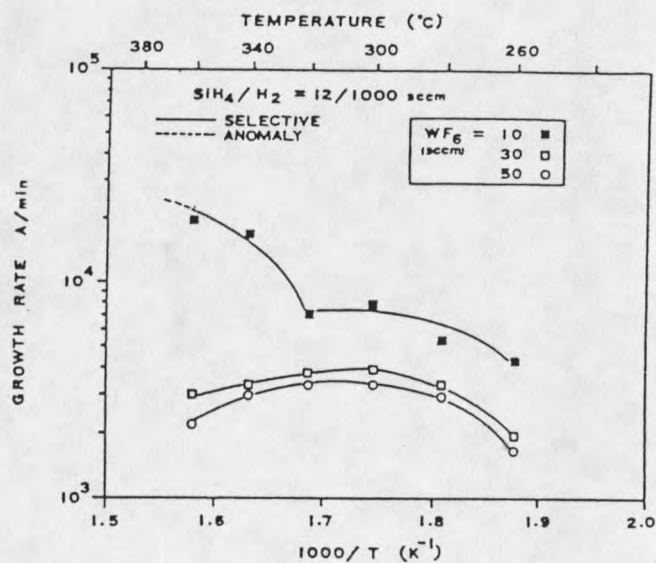


Figure 23. Arrhenius plots for $\text{SiH}_4\text{-WF}_6$ reaction system [7].

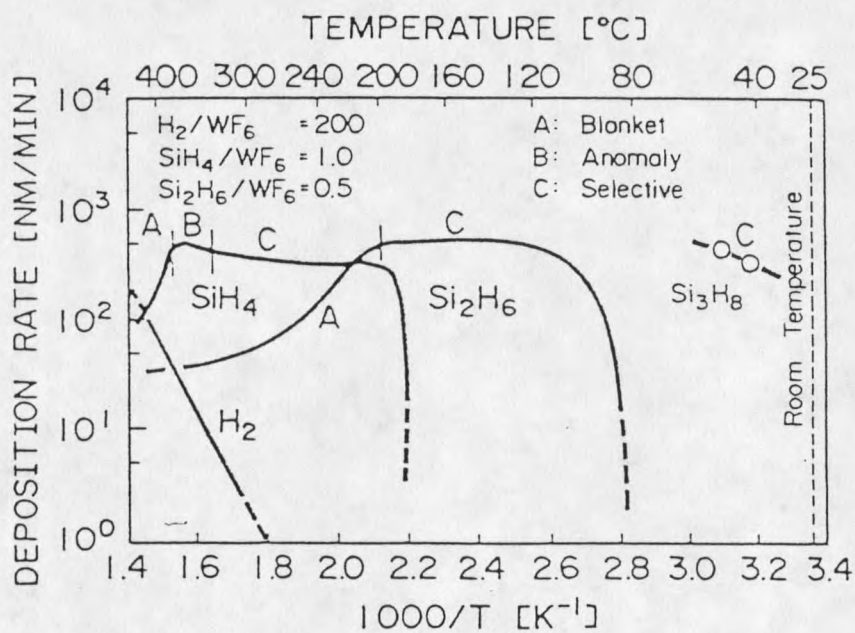


Figure 24. Arrhenius plot of H_2 and $\text{Si}_n\text{H}_{2n+2}$ ($n = 1-3$) reductions of WF_6 [8]: (A) blanket, (B) anomalous, and (C) selective deposition.

magnitude faster than that of H_2 reduction. There was no encroachment and leakage current of the resulting W deposit was low. They reported that the silane reduction reaction starts at around $180^\circ C$ and is mass transport limited within $180-280^\circ C$ range (Figure 24). The partial pressure dependence of the reaction was 1.3 with respect to silane ($R \propto P_{SiH_4}^{1.3}$) and 0.6 with respect to tungsten hexafluoride ($R \propto P_{WF_6}^{-0.6}$). The selectivity was lost at high SiH_4 partial pressures.

Schmitz, et al. [9] have performed experiments in a batch system to establish the kinetics of the SiH_4 reduction of WF_6 . They examined the temperature range between $250^\circ C$ and $550^\circ C$ under a total pressure of 0.075 torr. For SiH_4/WF_6 ratios less than 1.0, the rate expression was

$$R = \text{constant } (P_{WF_6})^0 (P_{SiH_4})^1 \quad (21)$$

However, the Arrhenius plot shown in Figure 25 is complicated, therefore they were not able to obtain an activation energy. Interpretation of the kinetic data led them to speculate that the homogenous dissociation of SiH_4 was the rate limiting step. In a subsequent study, Schmitz, et al. [104] reported that H_2 partial pressure as carrier gas has no influence on W growth rate or selectivity. This is in contrast with Kusumoto, et al. [7].

Rosler, et al. [10] have found that the selective W deposition rate was as high as $15,000 \text{ \AA}/\text{min}$ over the

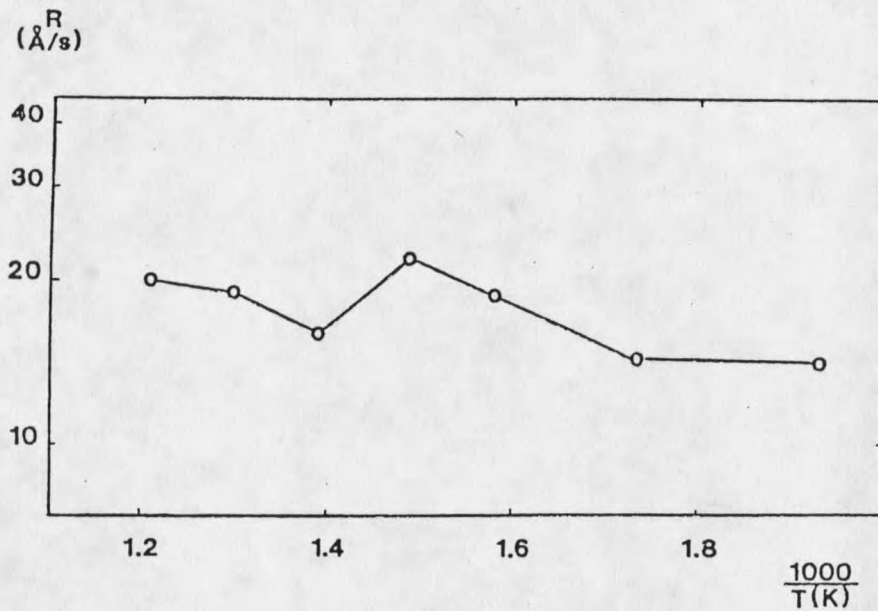


Figure 25. Arrhenius plot for $\text{SiH}_4/\text{WF}_6 < 0.9$ [9]. $P_{\text{tot}} = 75$ mtorr.

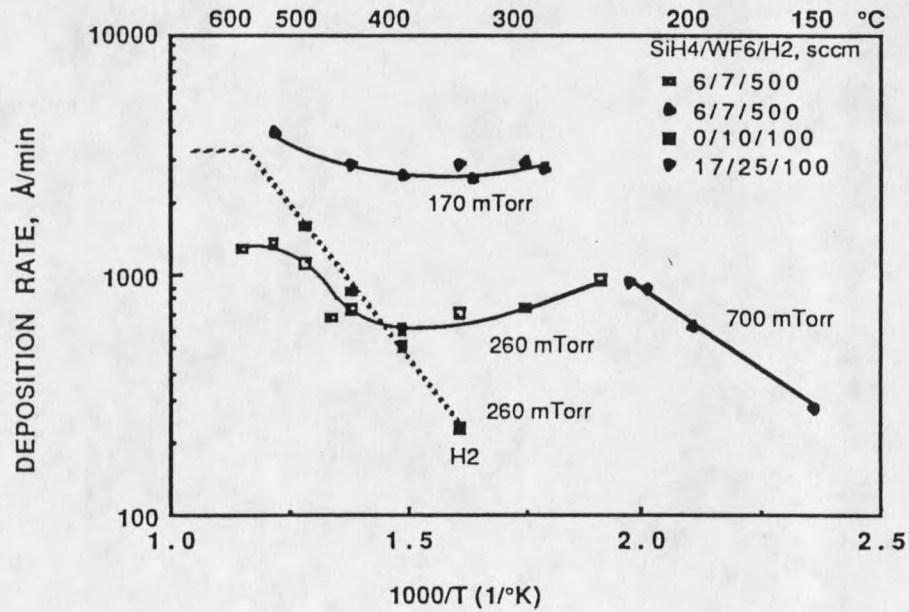


Figure 26. Arrhenius plot of blanket W deposition [10]. Comparison of H_2 and SiH_4 reduction. SiH_4 reduction at various flow rates and reactor pressures.

temperature range of 250-550°C, while the blanket W deposition rate was lower at low temperatures. They used a weight gain method to determine blanket deposit thicknesses, and SEM and step height measurements to determine selective W thicknesses in via holes. The Arrhenius plot for blanket deposition is given in Figure 26 and consisted of maxima and minima in a similar trend observed by Schmitz, et al. [9]. For a small temperature range between 150 and 200°C and at 0.7 torr, the activation energy was 0.28 eV/atom (26,780 Joule/mole). The rate expression was

$$R = k_0 e^{\frac{-E_a}{RT}} (P_{WF_6})^{-n} (P_{SiH_4})^1 \quad (22)$$

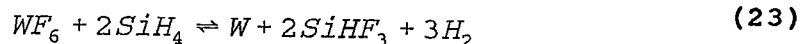
where, $n = 0-0.2$. They noticed that reactor pressure has an effect on the activation energy, and recommended that this effect be explored.

Ultra high vacuum (UHV) experiments by Yu, et al. [105] revealed that the reaction proceeds by repeating cycles of tungsten and silicon deposition. They used x-ray photoemission spectroscopy (XPS) to monitor the chemical species on the surface. The first cycle on the silicon surface is tungsten deposition through the reaction of WF_6 with silicon. Then, the deposition of silicon occurs by the reaction of SiH_4 with the fluorinated surface. Mass spectrometric studies showed that SiF_4 and H_2 are the major reaction products at low temperatures ($\sim 300^\circ C$). SiF_2 formation was observed at temperatures above $450^\circ C$ and HF formation at temperatures above $600^\circ C$. Since a

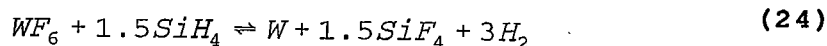
tungsten or a silicon seed layer on the substrate is the only requirement to start the tungsten deposition reaction with the $\text{SiH}_4\text{-WF}_6$ system, the substrate for the deposition is not restricted to silicon. Initial reactions of the $\text{WF}_6\text{-SiH}_4$ system with Al, PtSi and TiN surfaces have also been reported [106].

In another mass spectrometric analysis performed by Sivaram, et al. [107], it was confirmed that H_2 is the reaction product rather than HF for a Si/W ratio of less than 0.6 in the temperature range of 250-550°C. The absence of HF suggested that the SiH_4 decomposition results in molecular hydrogen (H_2), which desorbs without further reaction. The reaction was postulated to proceed by Si and H_2 formation on the surface and reaction of WF_6 with Si on the surface to form W. This is in agreement with the findings of Yu, et al. [104].

Kobayashi, et al. [108] used in situ Fourier transform infrared (FT-IR) spectroscopy and Auger electron spectroscopy (AES) to analyze the W formation reaction by the $\text{SiH}_4\text{-WF}_6$ reaction. They found that trifluoro-silane (SiHF_3), not SiF_4 , is the main by-product species, and proposed a new mechanism for the selective W deposition reaction. In a subsequent study, Kobayashi, et al. [109] introduced two reaction pathways and reported that by-product gases evolved during the reaction are a strong function of the SiH_4/WF_6 ratio. The proposed reaction pathways for the selective CVD region ($\text{SiH}_4/\text{WF}_6 < 1.0$) are



and



Reaction 23 was the dominant reaction for selective W-CVD on the silicon substrates.

Competitive adsorption of WF_6 and SiH_4 was believed to have an effect upon the reaction mechanism [104]. Growth rate versus WF_6 pressure profiles were supportive of this idea.

The initial stage of the tungsten formation reaction dictates the Si-W interface characteristics. Therefore, the electrical characteristics such as contact resistance and leakage current of a diffused layer are dependent on the initial reaction. Itoh, et al. [110] have analyzed the weight change versus deposition time data and speculated that there was a delay time at the initial stage of W deposition. Kajiyana, et al. [111] performed mass spectrometric analysis to evaluate the delay which occurs when SiH_4 is introduced into the reaction chamber as the first reactant. They related the delay time to the presence of the native oxide layer. NF_3 plasma treatment of Si surfaces removed the native oxide layer, and the delay time for nucleation was reduced.

Structural studies of CVD-W films with x-ray diffraction (XRD) analysis showed meta-stable β -W phase in addition to stable α -W and WSi_x phases. Reactions producing tungsten

silicide (WSi_x) are given in Table 1; their formation takes place at high SiH_4/WF_6 gas flow ratios.

Whereas β -W is a metastable phase of tungsten and is generally stabilized by the presence of impurity oxygen [112], α -W is a stable bcc tungsten phase [113]. The β -phase exhibits an A_3B (or A15) crystal structure [114], and the transformation of β -W to α -W is possible by heat treatment [115]. Table 2 contrasts α -W and β -W phases. Studies showed that β -W forms as a transition phase between α -W and WSi_x . Higher deposition temperatures and gas flow ratios of $\text{SiH}_4/\text{WF}_6 > 1.0$ resulted in β -W formation. Thermodynamic studies about the formation of W phases for SiH_4 - WF_6 reaction system are available in the literature [116,118].

Ohba, et al. [8] reported β -W formation when the SiH_4/WF_6 ratio was 4.0, and W_5Si_3 formation when the SiH_4/WF_6 ratio was 1.0 for temperatures above 380°C . Schmitz, et al. [104] observed α -W formation for $\text{SiH}_4/\text{WF}_6 < 1.3$, and β -W formation for $1.5 < \text{SiH}_4/\text{WF}_6 < 1.7$. Higher ratios yielded tungsten silicide deposition.

Tsutsumi, et al. [118] emphasized a critical value of the SiH_4/WF_6 ratio in order for the film structure to change from α -W to β -W. This value was between 0.4-1.0 and was dependent on the substrate materials examined (n^+Si , WSi_2 and TiSi_2).

The reactant ratio in the gas phase (SiH_4/WF_6) has an effect on the film morphology and impurity content. Tsutsumi, et al. [118] found that low SiH_4/WF_6 ratios delivered enough

Table 2. Tungsten Phases and Their Properties [114].

Phase	Structure	Lattice Constant, Å	Density, g/cm ³	Stability
α -W	bcc	3.165	19.3	stable
β -W	A15	5.036	19.1	metastable

lateral grain growth to form denser films, whereas high SiH_4/WF_6 ratios produced β -W films which contain larger amounts of oxygen and silicon. Ohba, et al. [119] have also found that the β -W films have higher impurity contents (e.g. F, O, Si) than do α -W films. Films of β -W exhibited porous structures and rough surfaces. Thus, β -W formation degraded the film conductivity. Nevertheless, overall, SiH_4 -reduced films were smoother than H_2 -reduced ones. Increasing temperatures and decreasing pressures produced smoother surfaces.

There have been studies to relate the resistivity to the impurity content of CVD-W films. Suzuki, et al. [120] used AES to analyze the Si content in the films. When Si concentration was less than 2 atomic %, Si dissolved substitutionally in α -W and the resistivity was proportional to Si concentration. When Si concentration was between 2-40 %, α -W and β -W were co-existent and the resistivity was not much affected by Si concentration. It was also speculated that Si segregates at the grain boundary of polycrystalline tungsten. Jeugd, et al. [121] employed AES and electron probe micro analysis (EPMA) to

elucidate resistivity dependence on the incorporated silicon. For $\text{SiH}_4/\text{WF}_6 = 1.0$, the increase in resistivity was $40 \mu\Omega\text{-cm/atomic \% Si}$. This was again explained by silicon segregation on the tungsten grain boundaries. On the contrary, Suzuki, et al. [122] stated that resistivity depends mostly on fluorine content, as determined by SIMS analysis, rather than silicon and oxygen content. Resistivity increased with increasing SiH_4 partial pressure and decreased with increasing temperatures down to $10 \mu\Omega\text{-cm}$ at 330°C . Ohba, et al. [119] reported that resistivity can be as low as $8 \mu\Omega\text{-cm}$ for W formed at 400°C (similar to the value obtained by H_2 reduction). This confirms Rosler's finding of $7.5\text{-}8.5 \mu\Omega\text{-cm}$ for deposition temperatures above 400°C [10].

Orientation of deposited films is another factor to be considered for kinetic evaluations. X-ray diffraction patterns in some research papers showed a (110) preferred orientation of tungsten crystals when $\alpha\text{-W}$ was the dominant phase [7,8,120]. In contradiction to these, Schmitz, et al. [9] reported a dominant (100) orientation for both $\text{H}_2\text{-WF}_6$ and $\text{SiH}_4\text{-WF}_6$ systems. Film orientation may be a result of deposition kinetics and/or be a cause in influencing the deposition kinetics of the subsequent layers. So far, no significant deliberation of this parameter has been available in the literature on W films formed from the $\text{SiH}_4\text{-WF}_6$ reaction.

A high film quality for VLSI technology requires that films have low stress values and have good adhesion to the

substrate. This is essential for a reliable device performance over a long period of time. Almost all films deposited are found to be in a state of internal stress regardless of the deposition method. The stress may be compressive or tensile [13]. The total stress in a film is the sum of: (a) the external stress on the film, usually from another film; (b) the thermal stress, resulting from the difference in the coefficients of thermal expansion between the film and the substrate; and (c) the intrinsic stress, which originates from the changes in the film structure. Saitoh, et al. [123] have reported that SiH_4 -reduced, CVD-W films have higher stress than do H_2 -reduced films. Ohba and Inoue [124] analyzed the stress for selectively deposited tungsten films. The film stress was a function of both deposition temperature and film thickness. When the wafers were heated from the back side, the stress changed from tensile to compressive as the deposition temperature and the film thickness increased. They observed that peeling occurred for the films deposited at low temperatures. This was in agreement with Rosler, et al. [10] since they reported excellent adhesion of W to Si at temperatures above 350°C .

CHAPTER 3

EXPERIMENTAL

Reaction SystemEquipment

A schematic diagram of the low pressure chemical vapor deposition (LPCVD) reaction system is given in Figure 27. Because of the hazardous characteristics of the gases used, the system is placed in a hood. The main parts of the system are: the gas lines and controllers, the reactor, the pressure controller, the pumps, the effluent gas treatment system, and the oil filtering system.

Gas Lines and Controllers: The gases used for the experiments are semiconductor-grade tungsten hexafluoride (WF_6), semiconductor-purity silane (SiH_4), and U.H.P. purity argon (Ar) as carrier gas. Specifications of the gases are given in Table 3; characteristics of the reaction gases and their hazards and handling are given in Appendix A. The tungsten hexafluoride line is kept heated to around $40^\circ C$ to reduce the possibility of condensation.

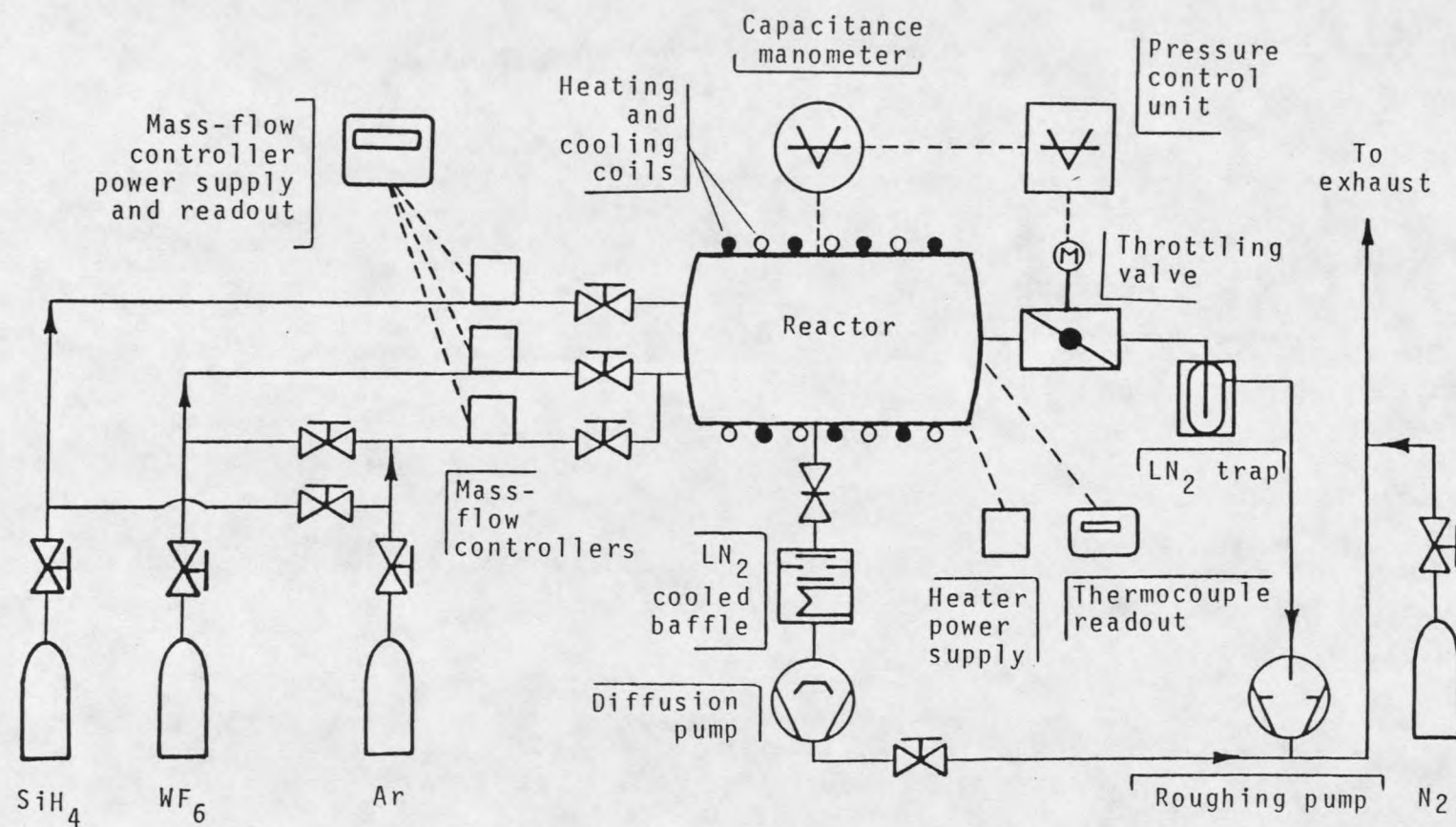


Figure 27. Schematic diagram of the LPCVD reaction system.

Table 3. Specifications of the Reaction Gases.

Gases	Component Specifications	
Tungsten hexafluoride (WF_6)	$\text{Ar} \ \& \ \text{O}_2 < 10 \text{ ppm}$	$\text{CO}_2 < 5 \text{ ppm}$
	$\text{HF} < 1,000 \text{ ppm}$	$\text{SiF}_4 < 10 \text{ ppm}$
	$\text{SF}_6 < 10 \text{ ppm}$	$\text{N}_2 < 10 \text{ ppm}$
	$\text{CF}_4 < 10 \text{ ppm}$	
Silane (SiH_4)	$\text{Ar} \ \& \ \text{O}_2 < 2 \text{ ppm}$	$\text{N}_2 < 2 \text{ ppm}$
	$\text{CH}_4 < 0.2 \text{ ppm}$	$\text{CO} < 1 \text{ ppm}$
	$\text{H}_2\text{O} < 1 \text{ ppm}$	$\text{CO}_2 < 1 \text{ ppm}$
	$\text{SiCl}_x < 1 \text{ ppm}$	
Argon (Ar)	$\text{O}_2 < 1 \text{ ppm}$	$\text{THC} < 0.2 \text{ ppm}$
	$\text{H}_2\text{O} < 1 \text{ ppm}$	

Three MKS type 1259 mass flow controllers and an MKS 247B four-channel readout and power supply unit are used to control the inlet gas flow rates. The controllable operation range for mass flow controllers are 0-120 sccm (standard cubic centimeters per minute) for tungsten hexafluoride, 0-305 sccm for silane, and 0-200 sccm for argon.

Reactor: The reactor system is a 6-way cross stainless steel vacuum chamber approximately 1.5 liters in volume. The reactor walls are wrapped with heating tapes and cooling coils

for bake-out and cold-wall reactor options, respectively. Figure 28 shows a cross-sectional view of the reactor.

The reactor is accessed by a flange on which the sample heater is attached. The sample heater is a copper block 6.3x6.3x1.3 cm in dimension with cartridge heaters. Silicon wafers are mounted on the block surface with screws from the wafer edges to ensure good conductive heating. Three 200-watt cartridge heaters, 7.6 cm in length and 0.95 cm in diameter, are inserted into the holes in the copper block assuring a good thermal contact. These cartridge heaters are connected in series and powered by a manually controlled 220-V variac.

Wafer temperature is measured by a 1/16 inch chromel (Type K) sheathed thermocouple mounted on the sample heater just beneath the wafer. This temperature is checked against a bare thermocouple placed on the copper block adjacent to the silicon wafer. These two readings agree within a 10°C temperature difference. It is observed that the calibration of the bare thermocouple changes during the reaction as the deposited tungsten layer on the junction point changes the thermocouple characteristics. Therefore, the sheathed thermocouple reading is taken as the reference for the experiments and corrected temperatures for the surface are reported.

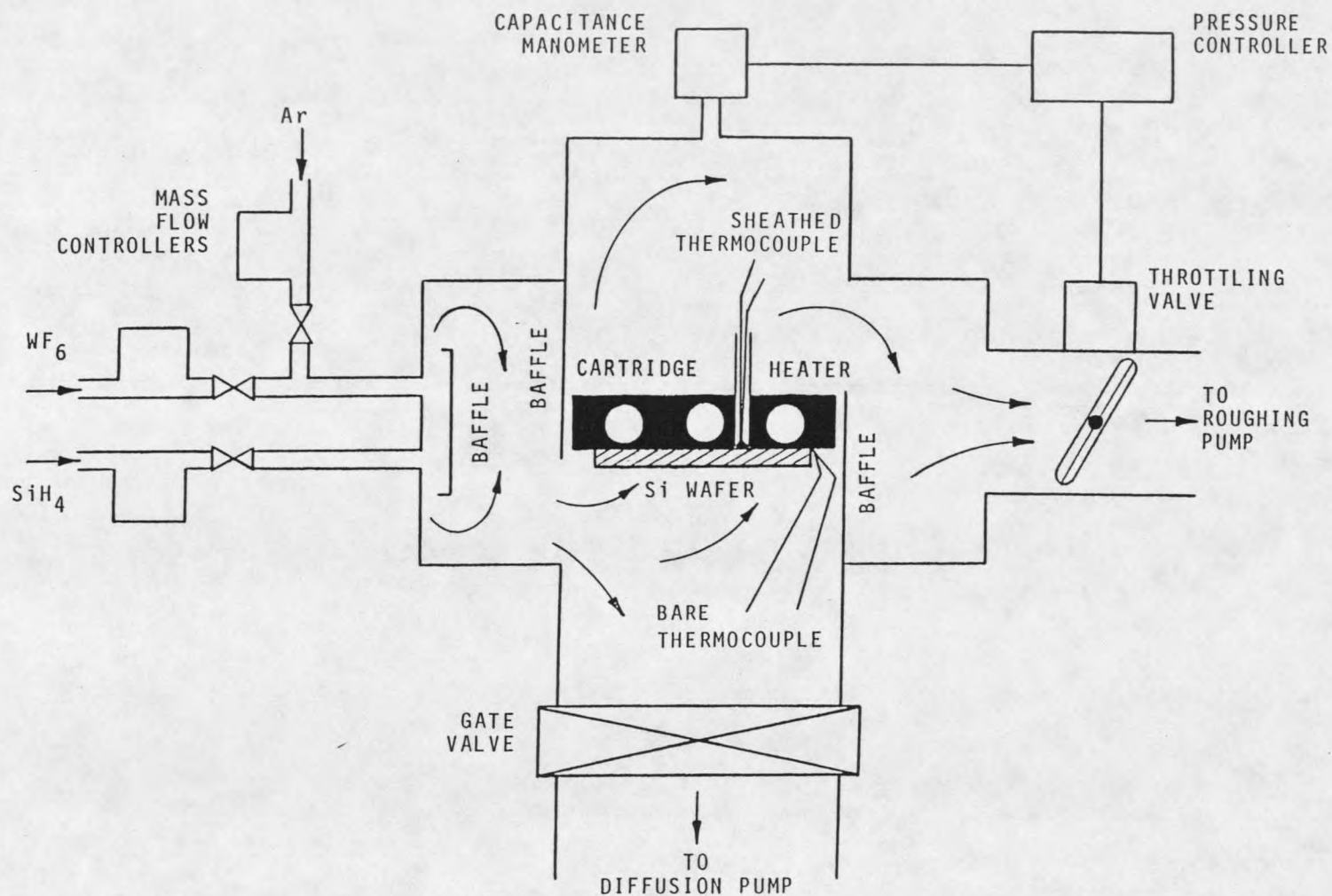


Figure 28. Cross-sectional view of the LPCVD reactor (substrate horizontal).

Pressure Controller: The reactor pressure is measured by a Type 12A MKS Baratron Vacuum Gauge. The readings are in terms of absolute pressures and the gauge has a range of 0.001-10 torr. The gauge is connected to an MKS PDR-D-1 Power Supply and Digital Readout unit. The system pressure is automatically regulated by an MKS Throttling Valve Type 253A-1-1-40-1. The throttling valve is a butterfly valve and is placed on the pumping line after the reactor. Pressure is regulated by varying the valve opening which in turn varies the pumping speed seen by the chamber. The throttling valve is powered and controlled by an MKS Type 252A Exhaust Valve Controller.

Pumps: The LPCVD system consists of one roughing pump and one diffusion pump.

The roughing pump is a Varian SD-300 Standard Series Mechanical Pump with two-stage direct drive. It has 310 l/min free air displacement and can deliver a vacuum of better than 10^{-4} torr. The pump is designed to provide vibration-free operation and is equipped with an anti-suckback valve to prevent oil from being sucked back into the vacuum system should the motor be stopped inadvertently. The pump is operated with Varian GP Type General Purpose Mechanical Pump Fluid.

A CVC-M60 diffusion pump is used for bake-out. The pump is air cooled and can pump down the system to 10^{-7} torr. A

liquid nitrogen-cooled baffle is placed between the diffusion pump and the chamber to prevent oil backstreaming into the chamber. Between the reaction chamber and the liquid nitrogen trap is a gate valve Model SVB-2.5V14, Torr Vacuum Products Inc. Varian Neovac SY Diffusion Pump Fluid is used in the pump.

Effluent Gas Treatment: The pyrophoric and corrosive natures of the reactant and product gases require special treatment before being purged into the exhaust hood. The treatment is carried out in two steps.

The first step is the condensation of reactor effluent gases by passing them through a liquid nitrogen trap, which is placed right after the throttling valve. The trap consists of a stainless steel cylinder, 10 cm in diameter and 20 cm in height, and is immersed in a liquid nitrogen container. The gas inlet and outlet pipes are 5 cm in diameter and are attached to the top flange. The inlet pipe goes inside the cylinder about 15 cm to require the gas to traverse a longer path inside the trap. The unreacted reactant and product gases except for H_2 and Ar condense at the liquid nitrogen temperature. This condensation action, in effect, serves as a cryopump, further increasing the pumping speed.

The second step is simply nitrogen dilution of gases right before the purge. Nitrogen gas is added to dilute the stream approximately 100 times at the roughing pump outlet.

Oil Filtering System: WF_6 forms hydrogen fluoride and a variety of tungsten oxides upon exposure to air. Tungsten oxide particles inside the roughing pump cause failure in the vanes. Thus, a continuous filtering and neutralization of the pump oil is necessary (Oil filtering system is not shown in Figure 27).

Some of the roughing pump oil is pumped by a MR1-23-49SM Simplex Milroyal Pump (a reciprocating, positive-displacement pump) to a Carquest Oil Filter 85050. The filter can retain particles as small as $10\text{ }\mu\text{m}$. The filtered oil is then sent to a neutralizer to remove the acidic fluorides. The neutralizer is a stainless steel cylinder 860 cm^3 in volume and is packed with Akzo Chemie Ketjen Catalyst, Silica-alumina ($SiO_2-Al_2O_3$) HA5P. The neutralized oil is passed through a rotameter, which also serves as a sight glass, and recycled back to the roughing pump. The pressure at the recycling pump outlet is continually monitored to make sure that the filter is not plugged. The filter and neutralizer packing is changed when the oil becomes darker.

Experimental Procedure

Sample Preparation

Before each experiment, reactor walls are wiped clean with methanol-dampened tissue.

One quarter of a 10-cm diameter (100) oriented boron- or phosphorus-doped silicon wafer is first washed with methanol to remove any organic residue on the surface. After rinsing with distilled water, the wafer is dipped in diluted 100:1 HF solution for 1 minute to eliminate the native oxide layer before the deposition. Elimination of the oxide layer is evidenced by a change in the attachment characteristics of distilled water on the silicon surface. Upon the elimination of the oxide layer, water has less tendency to attach to the silicon surface. The final cleaning is done with acetone and methanol wash. The cleaned wafer is then positioned on the substrate heater and is mounted in the reactor. Si substrates are positioned either vertically facing the reactor inlet or horizontally facing downward. In the vertical case, the baffles on both sides of the sample heater are removed (not shown in Figure 28).

Deposition

Reactor Preparation: After placing the sample in the reactor, initial pumpdown is done through the roughing line. When a vacuum better than 0.1 Torr is reached, the throttling

valve is closed and the chamber is pumped down through the diffusion pump line. The system is baked out at around 1×10^{-7} Torr for 60-90 minutes to remove the water vapor from the system. The bake-out temperature for the substrate and the reactor walls are $\sim 500^\circ\text{C}$ and $\sim 150^\circ\text{C}$, respectively. At the end of bake-out, the system is allowed to cool down to reaction conditions. Cooling of the reactor walls is facilitated by running water through the cooling coils.

After the cool-down, the gate valve is closed and the argon valve is opened for partial back-filling of the chamber. When the system pressure reaches about 0.1 Torr, argon flow is discontinued. The throttling valve is then opened to pump down the system through the roughing line. An increase in the system pressure before opening the throttling valve is necessary to prevent any back diffusion from the roughing line.

Before the reaction, the liquid nitrogen trap is filled, and time allowed for the temperature measured at the trap flange to drop to about -15°C . The substrate temperature and the system pressure are stabilized under argon flow. Meanwhile, the reactor walls are maintained at about 60°C to minimize WF_6 condensation which in turn may cause reactant depletion for the substrate.

Reactor Operation: After stabilization, SiH_4 and WF_6 are introduced into the chamber simultaneously and a chronograph is started. During the reaction, the substrate temperature is controlled manually through a variac to within $\pm 3^\circ\text{C}$. The reaction times vary from 0.5 minutes to 12 minutes. At the end of the reaction, the SiH_4 and WF_6 valves are manually closed at the same time, the throttling valve is completely opened, and the chronograph is stopped. The system is purged with argon for about 1 minute, then the argon valve is closed. During the argon purge, cooling water for the reactor walls is turned on to minimize any possible desorption of gases from the reactor walls and their subsequent adsorption on the substrate which could cause further reaction.

The substrate temperature is decreased at a rate lower than $5^\circ\text{C}/\text{min}$. Such a low rate does not impose high temperature gradients across the deposited W-Si interface that would contribute to delamination of the W layer (especially when the adhesion is poor). Under these conditions, the sample is allowed to cool below 45°C . The chamber is then filled with argon to atmospheric pressure, and the sample is taken out.

Data Analysis

For data evaluation, sheet resistance measurements, gravimetric measurements, SEM, XRD, and AES are used. Consistency in sampling is maintained by taking the samples

from similar locations on wafers for each analysis (e.g. from the center of the wafer for film thickness measurements).

Sheet Resistance Measurement

The sheet resistance values are directly measured by a 4-point probe. Measurements are performed on the whole one-quarter of wafer used for the deposition. The ranges of voltage and current used in measurements are 10-100 μV and 0.1-0.8 mA, respectively. During the measurements, the voltage is kept low so as not to induce local heating which could cause an increase in resistivity. The uniformity of the W film thickness is checked by performing sheet resistivity measurements at different locations on the wafer (one in the center and four on locations approximately 1 cm away from the edges of the wafer). All the measurements are taken at room temperature. Before proceeding with the rest of analysis, 1-cm wide blocks are cut off from the sides of wafers to minimize end effects.

Film Thickness Measurement

After the sheet resistance measurements, two samples, approximately 1.0x1.0 cm in dimension, are cut from the center of the wafer and weighed on a CAHN 29 Automatic Electrobalance. Then, the deposited tungsten layer is dissolved in 0.25M KH_2PO_4 / 0.24M KOH / 0.1M $\text{K}_3\text{Fe}(\text{CN})_6$ solution. It is necessary to heat the solution to boiling in

order to attain a reasonable etching rate. At the end of etching, samples are washed with distilled water, rinsed with acetone and dried prior to weighing. Successive etching and weighing processes are carried out until there is no significant change in weight. The total weight of the samples, depending on the size, varies in the range of 60-180 mg, while the weight loss is 0.2-19 mg. The electrobalance is sensitive to 1 μg weight difference in the working range of 1-250 mg. A Smiec Dial Caliper is used for area measurements. The caliper is sensitive to 0.00254 cm (0.001 in). The roughly rectangular samples are measured on each side and the average value for each opposing side is recorded. The area is then calculated assuming each sample to be a perfect rectangle. Knowing the area, A , and the weight loss after etching, Δm , tungsten film thickness, δ , is found from the formula

$$\delta = \frac{\Delta m}{\rho_b A} \quad (17)$$

A constant bulk density, ρ_b , of 19.3 g/cm is assumed throughout the calculations.

SEM Analysis

Samples for SEM analysis are cut to 0.3x1-cm dimension and are mounted on copper sample holder boats with a graphite adhesive solution. A JEOL-100CX Electron microscope with a scanning attachment equipped with ASID-4D is used for the analyses. The system has a lateral resolution of 30 Å. Plan-

view micrographs are taken at 20 keV primary beam energies and at 10,000x and 40,000x magnifications. Cross-sectional micrographs are taken at Applied Materials, Santa Clara, California. A 6,000x magnification is used.

AES Analysis

The AES surface analysis and depth profiling are carried out with a Physical Electronics, PHI 595 Scanning Auger Microprobe. The minimum electron beam size for the probe is 500 Å. The depth profiling is performed by rastering a 2x2 mm area for 30-second intervals. The argon (Ar^+) ion beam current and voltage for sputtering is $\sim 150 \mu\text{A}/\text{cm}^2$ and 3 kV, respectively. The primary electron beam voltage used is 3 keV with an accompanying beam current of $0.2 \mu\text{A}$. The data acquisition is achieved by a DEC PDP 11/04 computer. The sensitivity factors used for surface concentration analysis are given in Table 4 [125].

Table 4. AES Sensitivity Factors [125].

Si = 0.35	W = 0.055	O = 0.52
C = 0.2	F = 0.49	

X-ray Diffraction Analysis

X-ray diffraction analysis is performed on a General Electric XRD-5 diffractometer. X-ray source is Ni-filtered $\text{CuK}\alpha_1$ radiation ($\lambda = 1.54050 \text{ \AA}$) operated at 45 kV and 18 mA. Beam widths for the beam and detector slit widths are 1° and 0.2° , respectively. Medium range collimating assemblies are used for both the incident and reflected beams. Scanning speed of the Goniometer is $2^\circ 2\theta/\text{min}$ and chart speed is 1 in/min, giving a $2^\circ 2\theta/\text{in}$ diffractogram scale for the samples. Tungsten deposited Si wafers are scanned through a 2θ range of $30\text{--}80^\circ$. An approximate sample size of $2 \times 2 \text{ cm}$ is required for the analysis.

Scope of the Experiments

The SiH_4/WF_6 ratio, R , is kept constant throughout the experiments at 1.0 to favor $\alpha\text{-W}$ deposition over $\beta\text{-W}$ and tungsten silicide (WSi_x) deposition. The flow conditions for reactant gases are given in Table 5. "Horizontal" and "vertical" substrate positions are used in the experiments. The "horizontal" substrate position is shown in Figure 28 wherein the Si substrate faces downward, parallel to the overall flow across the chamber. The second baffle after the reactant entrance diverts the course of reactant gases toward the lower part of the chamber. The third baffle forces the reactants upward in the reactor where they can react on the Si

substrate surface. The reactant and product gases then leave from the upper chamber. In the case of the "vertical" substrate position, the substrate in Figure 28 is rotated 90° clockwise to face the reactant inlet. The second and the third baffles are removed. The "vertical" substrate position is therefore perpendicular to gas flow. The temperature and pressure dependence of the WF_6 - SiH_4 reaction and W films are analyzed in two parts:

(1) The first set of the experiments is designed to establish kinetic parameters while covering a temperature range as wide as possible ($\Delta T = \sim 250^\circ C$).

Substrate position : Horizontal, facing downward.

Reaction time : 4 minutes.

Temperature : 137-385°C.

Pressure : 1, 3, 10 torr.

(2) The second set of experiments is primarily designed to examine tungsten crystal growth trends with time, but also to evaluate the effect of substrate position on the kinetic parameters.

Substrate position : Vertical, facing reactant entrance.

Reaction time : 0.5-12 minutes.

Temperature : 285-385°C.

Pressure : 1, 10 torr.

Table 5. Gas Flow Conditions.

Substrate position	P (torr)	WF ₆ (sccm)	SiH ₄ (sccm)	Ar (sccm)
Horizontal	10	120	120	70
	3	110	110	64
	1	110	110	64
Vertical	10	110	110	64
	1	110	110	64

CHAPTER 4

RESULTS

The experimental results will be presented in six main sections. The first introduces the preliminary experiments for kinetic studies. The second presents the AES analysis findings on the impurity content of deposited films. The third includes the gravimetric analysis of the reaction rate and establishes the Arrhenius plot for the WF_6 - SiH_4 system. The fourth presents the SEM analysis of tungsten crystal morphology and growth patterns. The fifth reports x-ray diffraction analysis of tungsten phases and crystal orientation. The sixth explains the tungsten film resistivity in relation to film structure.

Preliminary Experiments

Reaction rates for tungsten deposition were found from the mass deposited at a corresponding reaction time using the gravimetric method. Equivalent film thickness was calculated from Equation 17. The calculations do not give the actual film thickness unless the film density is known. The method is suitable as far as kinetic studies and Arrhenius activation analysis are concerned since it directly gives the amount of tungsten formed. The resolution of the electrobalance used in weight measurements was 0.001 mg. The area of the chip samples

analyzed for W deposition was approximately 1 cm^2 . Therefore, when a constant W bulk density of 19.3 g/cm^3 is assumed, the equivalent thickness for continuous films could be predicted within $\pm 5 \text{ \AA}$. Deposition rate was found from the average thickness of W deposits. Two $1.0 \times 1.0 \text{ cm}$ Si chips were taken from the center of each wafer and an average film thickness was calculated. Average deviation in the rate was $\pm 10\%$ (maximum of $\pm 33\%$) for the horizontal substrate position and $\pm 6\%$ (maximum of $\pm 12\%$) for the vertical substrate position.

The expected effect of reactant gas flow rate on the deposition rate is discussed in Chapter 2. Prior to the final experiments on reaction kinetics, a set of experiments was conducted to find the flow rates of reactants for which the kinetics are free of starvation or mass flow rate limitations. These results are shown in Figure 29. The highest temperature, 385°C , for the project study range, which would give the highest deposition rate, was utilized. The flow rate for the kinetic studies was chosen from the region in which the deposition rate is independent of the flow rates. Gas flow rates for the horizontal substrate position were $\text{WF}_6 = \text{SiH}_4 = 120 \text{ sccm}$, $\text{Ar} = 70 \text{ sccm}$ for 10 torr total reaction pressure; $\text{WF}_6 = \text{SiH}_4 = 110 \text{ sccm}$, $\text{Ar} = 64 \text{ sccm}$ for 1 and 3 torr total reaction pressure. The reactor system has a limited pumping capacity; consequently, flow rates chosen for 3 and 1 torr

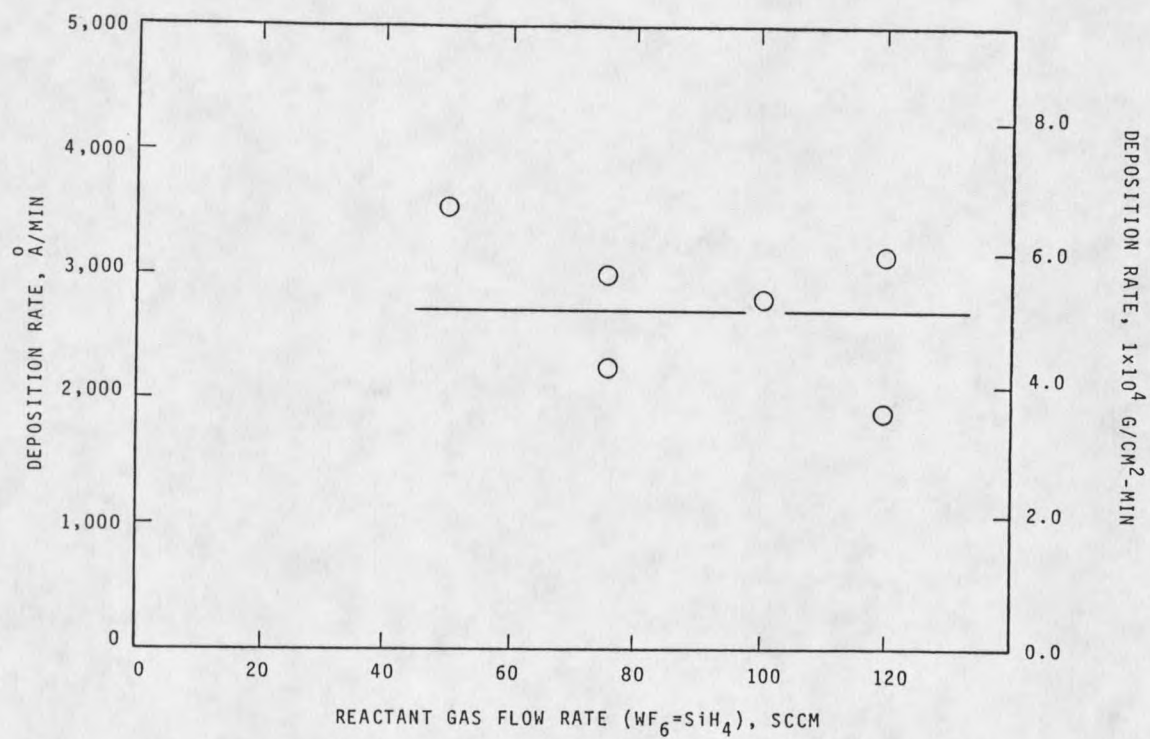


Figure 29. Preliminary experiments to assure differential reactor. (Horizontal substrate position, $P = 10$ torr, $T = 385^\circ\text{C}.$)

were lower than those for 10 Torr in order to attain the desired low pressures. Gas flow rates for the vertical position were constant for both 1 and 10 torr ($WF_6 = SiH_4 = 110$ sccm, Ar = 64 sccm).

Selectivite deposition of W on Si was tested by using 1.0 x 1.0-cm patterned wafers with 3500 Å oxide layers on the silicon. These wafers were placed next to Si(100) wafers on the substrate block. Tungsten deposition on both Si and SiO_2 (i.e. blanket W deposition) was observed within the experimental range studied.

AES Analysis

Impurity content of tungsten films was analyzed by Auger electron spectroscopy (AES). Possible atomic impurities are oxygen (O) from air, carbon (C) from CO or CO_2 from air and from back diffusion of pump oil, fluorine (F) from unreacted WF_6 or from undesorbed reaction products such as SiF_x or HF, and silicon (Si) from decomposition of SiH_4 or from undesorbed SiF_x . Si may also be present in the films as a result of silicide formation.

Auger depth profiles for tungsten films deposited at 10 torr-137°C, 1 torr-137°C, and 3 torr-385°C are given in Figures 30, 31, and 32, respectively. These samples are representatives of different deposition temperatures and presesures. The AES curves are from the samples with 4-minute

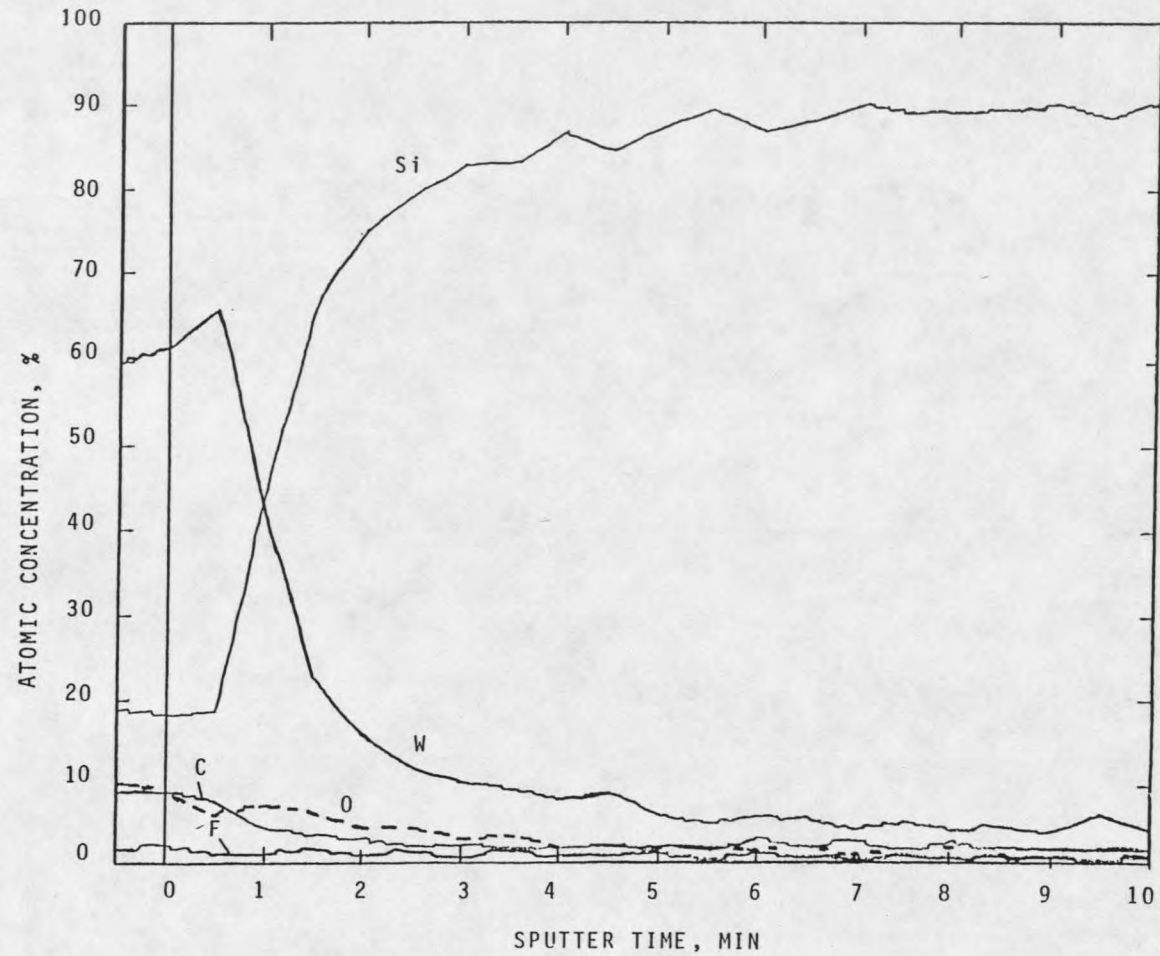


Figure 30. Auger depth profile for W film deposited at 10 torr and 137°C (t=4 min).

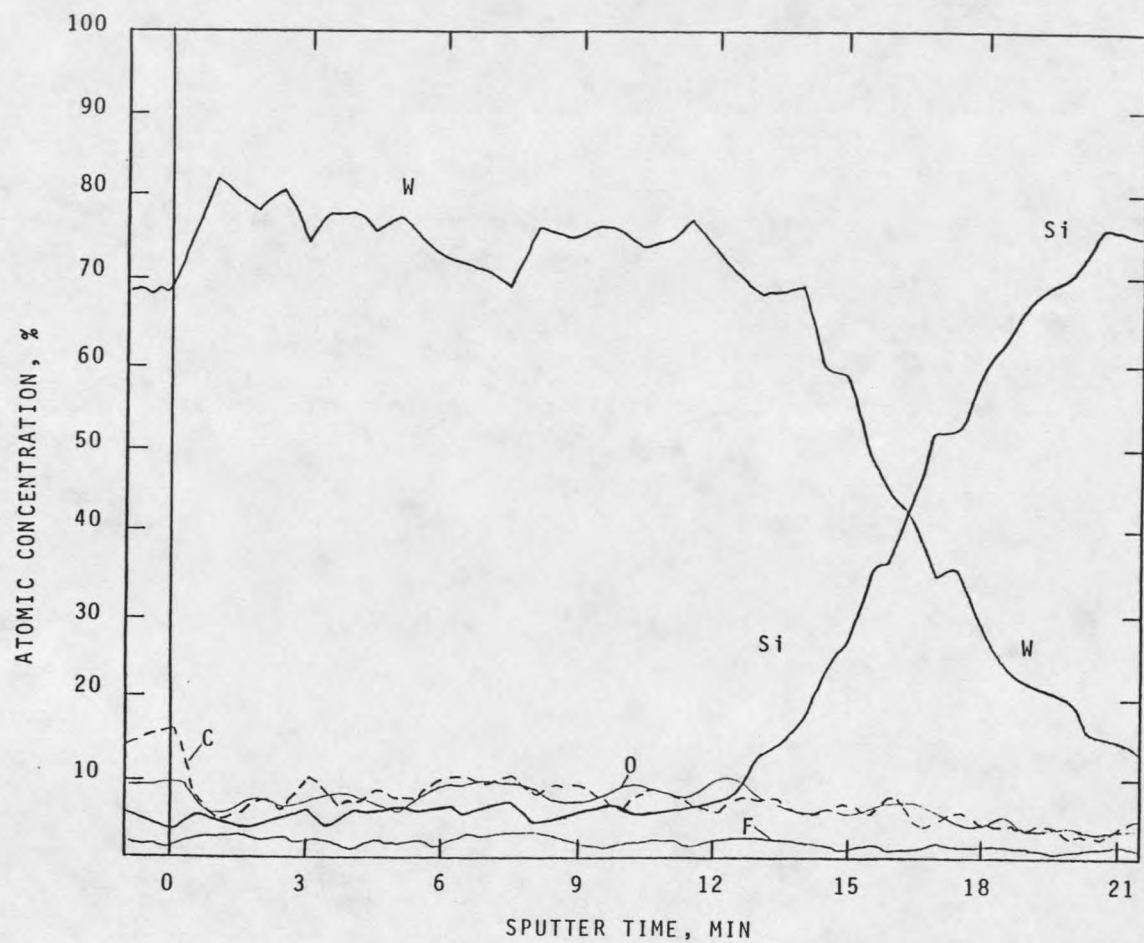


Figure 31. Auger depth profile for W film deposited at 1 torr and 137°C (t=4min).

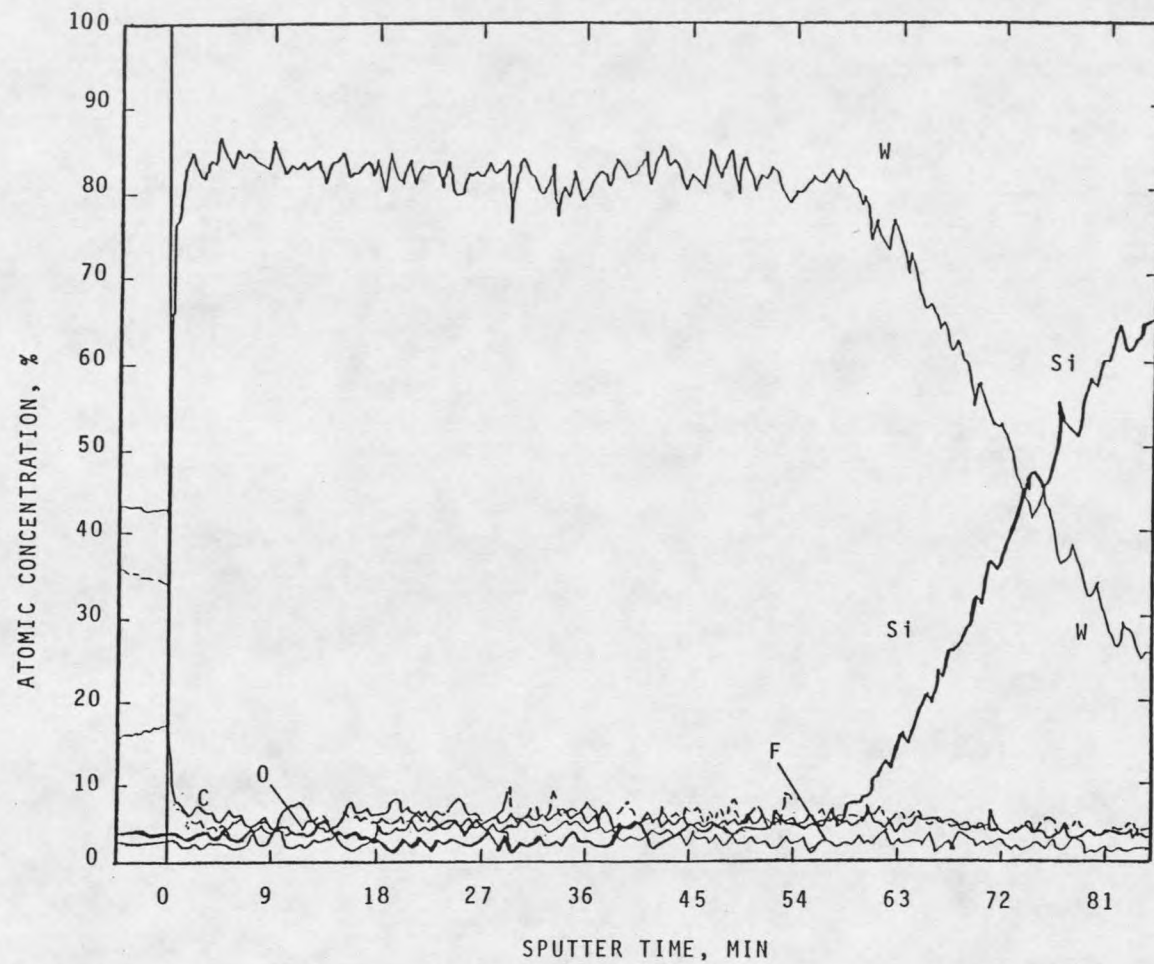


Figure 32. Auger depth profile for W film deposited at 3 torr and 385°C (t=4min).

reaction times. The Si-W interface is reached at longer sputter times for thicker films. Impurity contents in these films were within the noise level for Auger detection which was confirmed by a detailed analysis of the differential Auger spectra. Other analysis techniques, such as neutron activation analysis (NAA), electron probe micro analysis (EPMA), and secondary ion mass spectroscopy (SIMS) analysis are required to conclusively support the AES findings. However, there are no significant changes in atomic impurity concentrations throughout the film thicknesses. Another implication is that the low Si concentrations (practically in the noise level) excludes the presence of tungsten silicides in the films. Thus, the confirmed existence of only one reaction, tungsten formation, justifies one to proceed with the kinetic analysis of this particular reaction.

Other samples examined by AES depth profiling exhibited similar patterns. As explained in the SEM analysis section, the film deposited at 10 torr-137°C (Figure 30) was very thin and had a non-uniform W concentration distribution on the surface. Non-uniformity in W surface concentration was determined by observing different W concentrations on different locations on the surface by Auger analysis. High concentration sites probably correspond to initial nucleation sites implying that the film is primarily in the nucleation stage with minor surface diffusion under these reaction conditions.

Kinetics-Gravimetric

The thickness of the deposited tungsten ranged from 300 to 88,000 Å. The Arrhenius plot for $\text{SiH}_4\text{-WF}_6$ reaction system is given in Figure 33. The data correspond to 4-minute reaction times. It is quite striking to see that the apparent activation energy changes with system pressure, which is contrary to the $\text{WF}_6\text{-H}_2$ system [5]. The apparent activation energies are 0.35 eV/atom (33,300 J/mole) for 10 torr, 0.17 eV/atom (16,600 J/mole) for 3 torr, and 0.08 eV/atom (7,800 J/mole) for 1 torr. Different activation energy values for different pressures indicate that the rate controlling mechanism changes with pressure. The data presented in Figure 33 are for the horizontal sample position (substrate surface facing downward). Similar activation energy behavior was also observed in Figure 34 with sample in the vertical position (facing the reactant inlet). The data for 1- and 1.5-min reaction times are presented in Figure 34. The results for 0.5-min reaction time have been determined to be not suitable for kinetic studies and are excluded. The reason is that it takes approximately 15-20 seconds for the system pressure to stabilize after the introduction of reactants, thus a 30-second reaction time is far from representing a steady state reactor operation. Activation energies presented in Figure 34 are for the films which are still in the island/coalescence stage. The vertical substrate position yielded higher

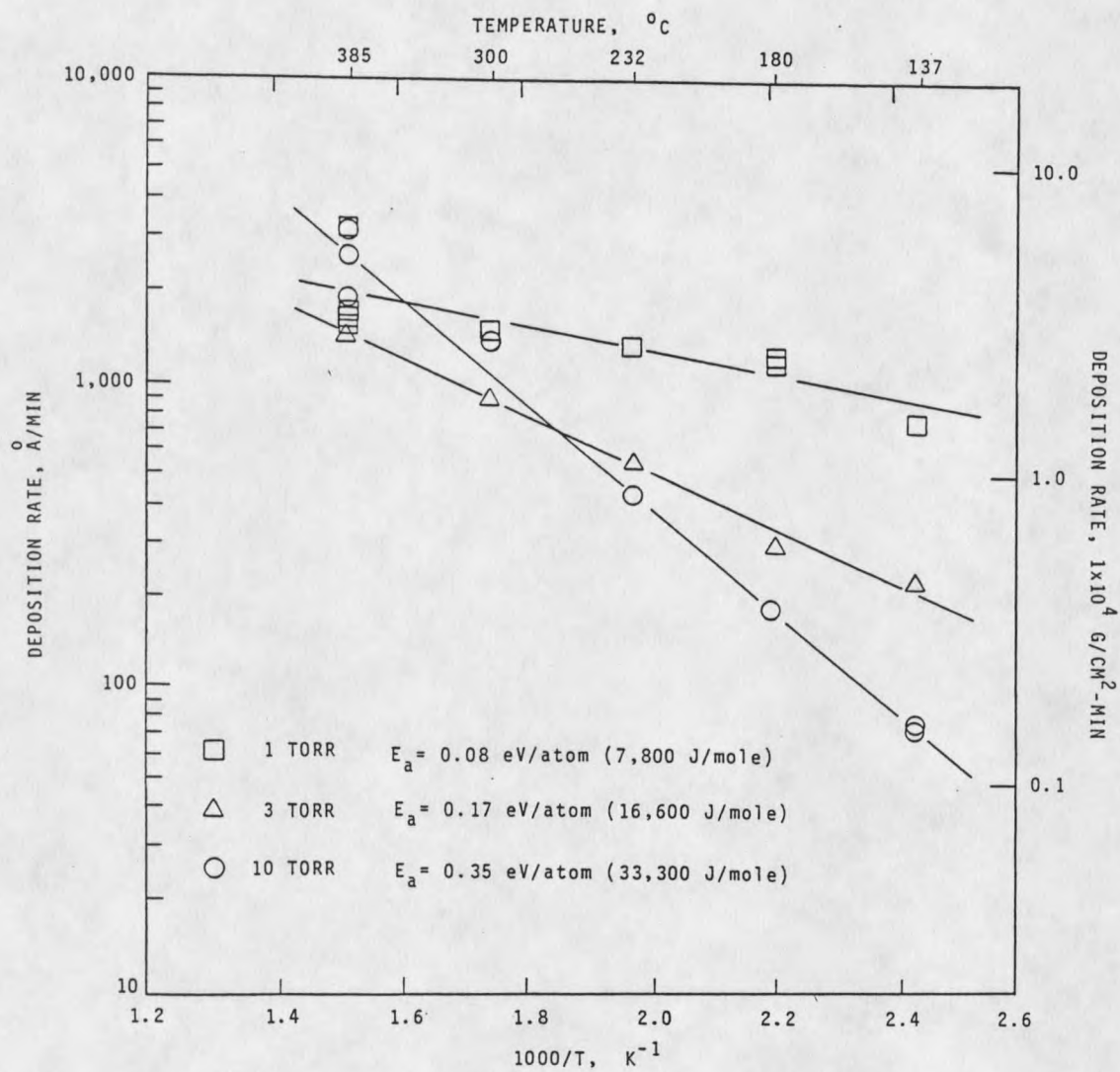


Figure 33. Arrhenius plot for $\text{WF}_6\text{-SiH}_4$ system. Substrate horizontal, $t = 4$ min.

activation energies than did the horizontal substrate position. The apparent activation energies for the vertical position are: 0.40 eV/atom (38,300 J/mole) for 10 torr, and 0.12 eV/atom (11,420 J/mole) for 1 torr. The average rates for longer reaction times (10-12 minutes) are shown also. Dashed lines in Figure 34 are provided as visual aids only, they do not represent a fit for data. Note that 10 to 12-minute reaction times correspond to a rate for continuous film formation where reaction surface area and crystal orientation are different from those of the island/continuous film stage. Evidently, the deposition rate changes with film thickness. This is discussed together with SEM and XRD analysis results later.

SEM Analysis

Experiments for SEM analysis were conducted in two parts: time-dependent experiments for kinetic studies and experiments to form thick films for morphological studies. Additionally, the original experiments with tungsten films grown for 4 minutes were analyzed by SEM.

Time-dependent Experiments

A set of reaction-time-dependent experiments was performed to analyze the crystal growth habits. Individual aggregate sizes were measured by using SEM plan-view

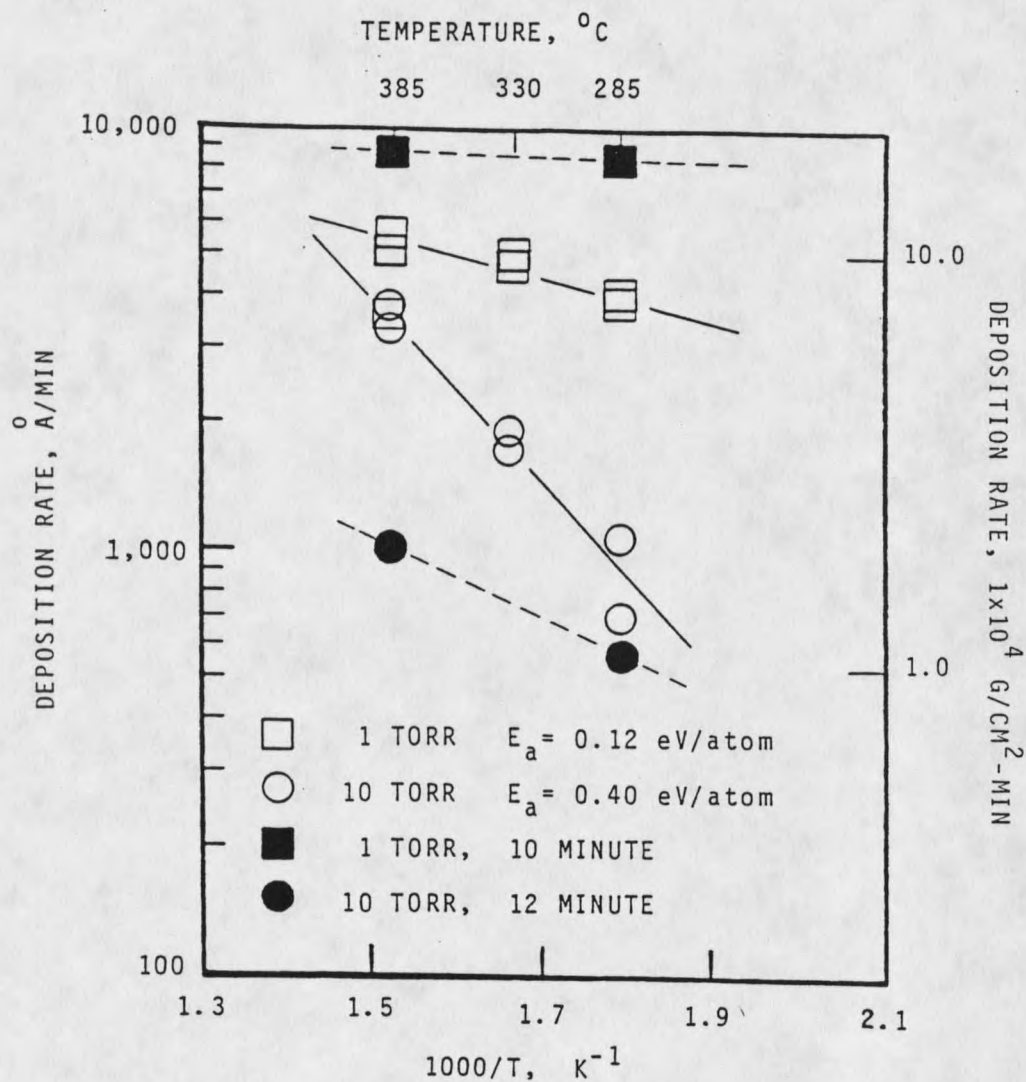


Figure 34. Arrhenius plot for $\text{WF}_6\text{-SiH}_4$ system. Substrate vertical; ○ and □ $t = 1\text{-}1.5$ min, ● and ■ $t = 10\text{-}12$ min.

micrographs of tungsten surfaces. An average aggregate size was determined for each deposition condition.

Figure 35 shows how the aggregates grow with time for the deposition condition of 10 torr and 385°C. At 0.5 min, islands have already formed and some of them have grown vertically more than the others. This stage shows very limited lateral growth. At 1.0 min, aggregates are bigger and they show more crystalline structure with sharper geometries. The film appears highly porous. At 12 min, aggregates have had enough time to grow and touch each other. A complete coalescence at the 12-min deposition time is not observed; however, porosity appears lower than that at smaller deposition times.

Figures 36 and 37 show tungsten film surfaces deposited at temperatures of 285, 330 and 385°C for 1.5 minutes at 10 torr and 1 torr, respectively. Aggregate sizes for 1 torr are larger than those for 10 torr. This is a result of higher deposition rates at lower pressures. Within 1.5 minutes under the reaction conditions the tungsten surfaces are still in the island/coalescence stage except for the film deposited at 1 torr-385°C (The deposition rate at this condition was high enough to form a continuous film in 1.5 min). The complete set of SEM micrographs for the time dependent experiments are included in Appendix H.

Average aggregate size versus reaction time data are presented in Figures 38 and 39 for 10 torr and 1 torr, respectively. The average aggregate sizes for reaction

